

Final Report on Investigating Grain Dynamics in Irradiated Materials with High-Energy X-rays

Nuclear Science and Engineering Division

About Argonne National Laboratory

Argonne is a U.S. Department of Energy laboratory managed by UChicago Argonne, LLC under contract DE-AC02-06CH11357. The Laboratory's main facility is outside Chicago, at 9700 South Cass Avenue, Argonne, Illinois 60439. For information about Argonne and its pioneering science and technology programs, see www.anl.gov.

DOCUMENT AVAILABILITY

Online Access: U.S. Department of Energy (DOE) reports produced after 1991 and a growing number of pre-1991 documents are available free at OSTI.GOV (<http://www.osti.gov/>), a service of the US Dept. of Energy's Office of Scientific and Technical Information.

Reports not in digital format may be purchased by the public from the National Technical Information Service (NTIS):

U.S. Department of Commerce
National Technical Information Service
5301 Shawnee Rd
Alexandria, VA 22312
www.ntis.gov
Phone: (800) 553-NTIS (6847) or (703) 605-6000
Fax: (703) 605-6900
Email: **orders@ntis.gov**

Reports not in digital format are available to DOE and DOE contractors from the Office of Scientific and Technical Information (OSTI):

U.S. Department of Energy
Office of Scientific and Technical Information
P.O. Box 62
Oak Ridge, TN 37831-0062
www.osti.gov
Phone: (865) 576-8401
Fax: (865) 576-5728
Email: **reports@osti.gov**

Disclaimer

This report was prepared as an account of work sponsored by an agency of the United States Government. Neither the United States Government nor any agency thereof, nor UChicago Argonne, LLC, nor any of their employees or officers, makes any warranty, express or implied, or assumes any legal liability or responsibility for the accuracy, completeness, or usefulness of any information, apparatus, product, or process disclosed, or represents that its use would not infringe privately owned rights. Reference herein to any specific commercial product, process, or service by trade name, trademark, manufacturer, or otherwise, does not necessarily constitute or imply its endorsement, recommendation, or favoring by the United States Government or any agency thereof. The views and opinions of document authors expressed herein do not necessarily state or reflect those of the United States Government or any agency thereof, Argonne National Laboratory, or UChicago Argonne, LLC.

Final Report on Investigating Grain Dynamics in Irradiated Materials with High-Energy X-rays

Prepared by

Meimei Li¹, Xuan Zhang¹, Jonathan D. Almer², Jun-Sang Park², Peter Kenesei²

¹Nuclear Science and Engineering Division, Argonne National Laboratory

²X-ray Science Division, Argonne National Laboratory

December 2019

EXECUTIVE SUMMARY

This report summarizes the research activities conducted at the Argonne National Laboratory (ANL) under the FY 2016 Consolidated Innovative Nuclear Research (CINR) Funding Opportunity Announcement (FOA) award CFA-16-10644: Investigating Grain Dynamics in Irradiated Materials with High-Energy X-rays. This project is a collaboration between the ANL and the Los Alamos National Laboratory (LANL). The research activities conducted at the LANL is summarized in the companion report, LA-UR-19-29312 titled “EVPSM Modeling of 316 Stainless Steel with and without Observed Phase Transformation.”

The project aims to develop a capability for conducting a multiscale experiment on an irradiated material enabled by high-energy X-rays by integrating *in situ* mechanical loading with a suite of high-energy X-ray techniques. The focus is on 3D microstructural characterization *in situ* to investigate grain dynamics in irradiated materials. A custom-made μ TS5 - 5 kN micro test system was developed for conducting *in situ* tensile tests of radioactive specimens with 3D high-resolution far-field High-energy X-ray Diffraction Microscopy (ff-HEDM) and tomography at the beamline 1-ID at the Advanced Photon Source (APS). A case study on neutron-irradiated Fe-9Cr specimens is presented, including *ex situ* near- and far- field HEDM and tomography before *in situ* tensile tests, *in situ* tensile tests with ff- HEDM and wide-angle X-ray scattering (WAXS), and *ex situ* near- and far-field HEDM and tomography after *in situ* tensile tests for neutron-irradiated Fe-9Cr specimens. Also discussed is *in situ* elevated-temperature tensile tests of a neutron-irradiated high-temperature, ultrafine-precipitate strengthened (HT-UPS) stainless steel using the *in situ* **Radioactive Materials** (iRadMat) characterization apparatus. These new capabilities open up new opportunities for the nuclear material community to study complex reactor materials at multiple length scales, allowing for bridging a wide range of length scales that are inherent in the deformation and failure processes in irradiated materials. We also proposed to build an Activated Materials Laboratory (AML) next to the new long beamline, High-Energy X-ray Microscope (HEXM) at the APS, as part of the APS-Upgrade Project. The AML will facilitate the access to these advanced characterization tools by the nuclear community.

TABLE OF CONTENTS

EXECUTIVE SUMMARY	ii
TABLE OF CONTENTS.....	iii
1 Introduction	1
2 3D Characterization of Neutron-Irradiated Specimens with <i>in situ</i> Tensile Loading	2
2.1 Capability Development	2
2.2 Case Study: <i>in situ</i> tensile test of neutron-irradiated Fe-9Cr alloy	4
2.2.1 <i>Ex situ</i> near- and far- field HEDM and Tomography of Neutron-Irradiated Fe-9Cr Alloy before <i>in situ</i> Tensile Test.....	4
2.2.2 <i>In situ</i> tensile test with far-field HEDM and WAXS of Neutron-Irradiated Fe-9Cr Alloy	9
2.2.3 <i>Ex situ</i> near- and far- field HEDM and Tomography of Neutron-Irradiated Fe-9Cr Alloy after <i>in situ</i> Tensile Test.....	17
3 <i>In situ</i> Elevated-Temperature Tensile Tests of Neutron-Irradiated Specimens Characterized with High-Energy X-rays	21
4 Activated Specimens Handling and Proposed Activated Materials Laboratory (AML) at the APS.....	24
5 Summary	27
Acknowledgement	28
References.....	28

1 Introduction

The development and deployment of advanced nuclear energy systems is critically dependent on advanced high performance materials that can tolerate extreme conditions of radiation, high temperature, stress, and corrosive environments. Life extension of existing nuclear power plants heavily relies on understanding of radiation-induced degradation in materials properties during long-term service. Designing radiation, heat and corrosion-resistant materials and predicting the response of materials in extreme nuclear environments are grand challenges for future growth of nuclear energy.

Radiation damage is a classical multi-scale physics problem. Irradiation produces a large concentration of point defects and defect clusters in a crystalline solid at the atomic scale and in pico-seconds. Further evolution of these defects leads to formation of various types of extended defect structures, such as dislocation loops, dislocation network, stacking fault tetrahedra, voids, and helium bubbles, as well as precipitates, and phase transformations that impact the integrity and lifetime of nuclear reactor components [1]. Prediction of mechanical properties of materials under irradiation requires a fundamental understanding of material behavior across a range of time and length scales. This multiscale complexity has limited the prediction to a few simple cases and model configurations. Modeling the relationship between the state of microstructure and the deformation and damage mechanisms has remained largely phenomenological. The challenge is to capture the fundamental physical processes of the evolution of various types of microstructural barriers, and understand the interactions of these individual micro-processes, to determine the macroscopic mechanical response under service conditions. While multi-scale models are being actively developed, there is a lack of multiscale experimental data for validation and improvement of these models. The combined application of closely-coupled multiscale modeling and multiscale experimentation is key to the understanding and prediction of how the nano- and micro-scale structural evolution is linked with the macroscale response in a material.

An ideal multiscale experiment requires combining a suite of techniques to analyze the material behavior at multiple scales in a single experiment to develop an integrated and accurate view of the structural interactions across the scales. Opportunity for such an experiment has arisen from the rapid advance of high-energy X-ray techniques offered at synchrotron radiation facilities. The high penetrating power of high-energy X-rays allows a millimeter-sized specimen tested *in situ* under thermal-mechanical loading to obtain reliable macroscale stress-strain behavior without compromise of bulk property measurements [2]. Deformation and failure mechanisms in a multi-component, multi-phase engineering material can be elucidated at several length scales using multiple X-ray techniques. For instance, internal stresses in different phases, dislocation evolution, and nano-scaled void formation and growth in a ferritic-martensitic steel were revealed by simultaneous measurements of wide-angle X-ray scattering (WAXS) and small-angle X-ray scattering (SAXS) during tensile deformation [3,4]. Strain and texture mapping around a crack tip using *in situ* synchrotron X-ray diffraction (XRD) provided a better understanding of deformation and crack propagation mechanisms under static and fatigue loading [5]. Recently-developed high-energy diffraction microscopy (HEDM) (also known as 3D XRD) can measure the micro-mechanical states in each of hundreds to thousands of grains within a polycrystalline aggregate. This grain-scale interrogation revolutionizes the conventional measurements of average behavior of grain ensembles of materials, providing unprecedented details of grain dynamics crucial to the understanding of the effect of microstructural inhomogeneities on the macroscopic behavior of polycrystalline materials [7]. Combined imaging studies, such as grain structure mapping by

diffraction contrast tomography and crack mapping by synchrotron X-ray micro-tomography (μ -CT) provided new insight into the dynamic interaction of a growing crack with crystal structure and the contribution of different boundary types to cracking resistance in corrosive environments [7]. The synergy of WAXS, SAXS, HEDM, μ -CT and *in situ* thermal-mechanical loading offer promises in probing structure over a range of length-scales, from angstroms to mm, mapping variations in grain characteristics including their positions, volumes, orientations, shapes, strains, and dislocation densities, voids and cracks, to paint a robust picture of material evolution. These advanced X-ray techniques when applied to post-irradiation examination of nuclear materials, hold enormous potential for understanding and predicting the mechanical performance of materials in nuclear reactor environments.

This project aims to develop the capability for conducting a multiscale experiment on an irradiated material enabled by high-energy X-rays. *In situ* mechanical loading of an activated specimen is integrated with a suite of high-energy X-ray techniques developed by the X-ray community with the focus on 3D microstructural characterization by far-field HEDM to investigate grain dynamics in irradiated materials. This new capability will open up new opportunities for the nuclear material community to study complex reactor materials at multiple length scales in a single experiment, and bridge a wide range of length scales that are inherent in the deformation and failure processes in irradiated materials. We also propose to build an Activated Materials Laboratory (AML) that will facilitate the access to these advanced characterization tools by the user community, particularly for effective use of the specimen library provided by the DOE Nuclear Science User Facilities (NSUF).

2 3D Characterization of Neutron-Irradiated Specimens with *in situ* Tensile Loading

2.1 Capability Development

A custom-made μ TS5 - 5 kN micro test system was developed in this project for conducting *in situ* tensile tests of radioactive specimens with 3D high-resolution far-field High-energy X-ray Diffraction Microscopy (ff-HEDM) and tomography at the beamline 1-ID at the Advanced Photon Source (APS). The test system was made by Psylotech. The main components include a mechanical frame, a miniaturized roller screw actuator, a strain gauge load cell, a universal testing hub, and a control unit with Psylotest software. The load capacity is 5kN.

To test radioactive specimens using the micro test system at the APS, the radioactive specimen must be properly contained to prevent radiation contamination during the entire experimental period. An adequate radiation shielding is also required to minimize radiation exposure to personnel. A set of grips with a double-layered kapton tube containment was designed to provide a primary containment for the radioactive specimen, as shown in Fig. 1. The grip set can be used for room-temperature tensile tests of two different types of subsized sheet-type tensile specimens given in Fig. 2. A secondary containment was designed to enclose the entire micro test frame when testing a radioactive specimen at the beamline, as shown in Fig. 1. This grip assembly and secondary containment allows handling of low-activity specimens in a designated control area (specimen exposure < 5 mR/h @ 30 cm). An exterior radiation shielding is required for handling and testing higher-activity radioactive specimens (specimen exposure > 5 mR/h @ 30 cm). The primary and secondary specimen containments have been approved by the APS Radioactive

Specimen Safety Review Committee (RSSRC) and are routinely used for testing radioactive specimens at the APS.

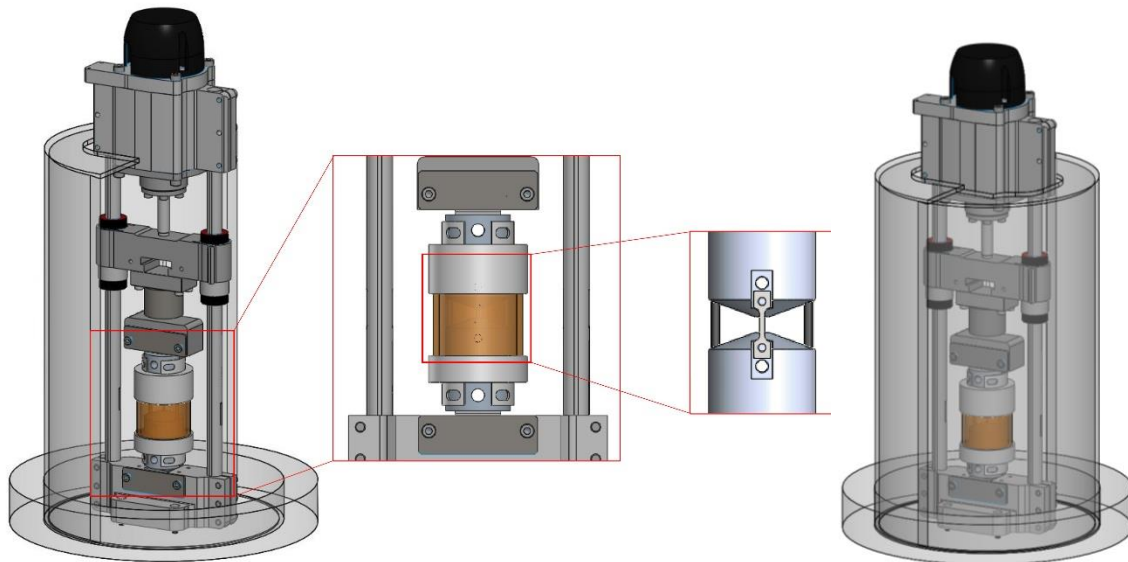
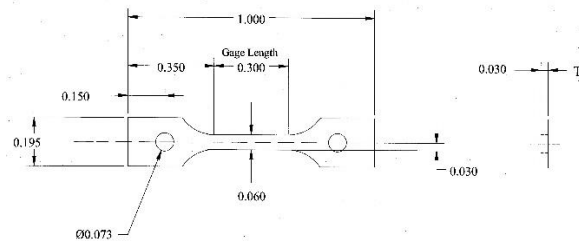
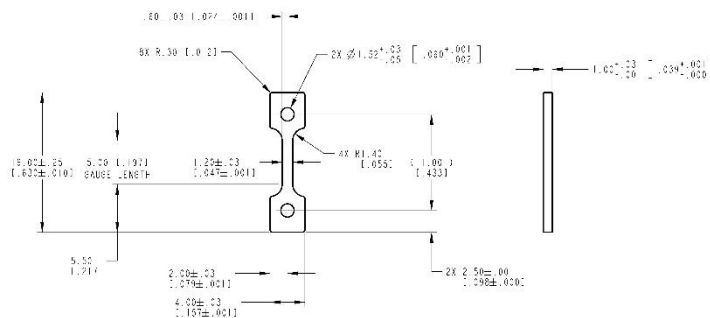


Figure 1. 3D models showing the grip assembly for a radioactive specimen installed in the Psylotech micro test frame. The radioactive specimen is contained in a double-layered kapton tube for a room-temperature tensile test. The micro test frame is enclosed in a plastic secondary containment.



(a)



(b)

Figure 2. Two types of subsized sheet-type tensile specimens: (a) total length of 25 mm, and (b) total length of 16 mm.

2.2 Case Study: *in situ* tensile test of neutron-irradiated Fe-9Cr alloy

2.2.1. *Ex situ* near- and far- field HEDM and Tomography of Neutron-Irradiated Fe-9Cr Alloy before *in situ* Tensile Test

Experimental Procedure

Near-field and far-field HEDM and X-ray tomography was carried out at the APS beamline 1-ID on three subsized sheet-type tensile specimens of an Fe-9Cr alloy, unirradiated, neutron irradiated to 0.1 dpa at 300 and 450°C, respectively. These three specimens were subsequently tensile tested *in situ* with far-field HEDM and WAXS measurements that are described in the following section. The schematic drawing of the specimen is given in Fig. 2(b). The nominal gage dimensions of the specimens were 1.2 mm (width) × 0.5 mm (thickness) × 5 mm (length) with a total length of 16 mm. The experimental setup for the nf- and ff-HEDM at the beamline 1-ID is shown in Fig. 3. The irradiated specimen was encapsulated in double-layered Kapton tubes.

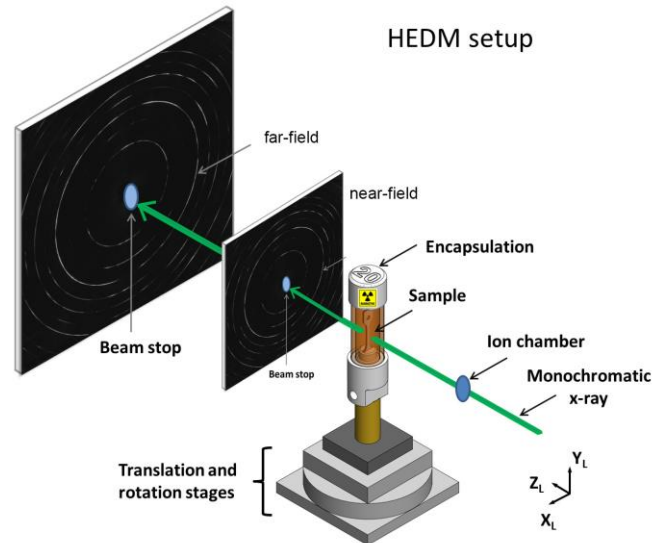


Figure 3. Experimental setup for *ex situ* near-field and far-field HEDM of a radioactive specimen at the APS beamline 1-ID.

The beam energy, beam size and the specimen-to-detector (SD) distance for nf- and ff-HEDM and X-ray tomography are given in Table 1. Tomography and ff-HEDM used box beams, and nf-HEDM used focused beams. Because the beam height of the focused beams for nf-HEDM was only 2 μm , each measured layer sampled a plane in the specimen cross section. Therefore, a number of layers were measured by nf-HEDM to sample a larger volume of the specimen. For the unirradiated specimen, 65 layers were measured by translating the specimen vertically along the specimen gage direction. Multiple scans were conducted with the step size of 5 μm . The two irradiated specimens were measured in a similar fashion, and a total of 129 layers were measured. For all three specimens, the middle layer of the nf-HEDM measurements was located at the center of the specimen gage. The total volume measured by nf-HEDM was covered in two layers of the ff-HEDM measurements using box beams.

Table 1. Parameters for nf- and ff-HEDM and tomography measurements.

Specimen	Energy (keV)	Beam size (mm × mm)	SD distance (mm)	Measurement
Unirradiated	65.351	1.8 × 1 - tomo; 1.8 × 0.16 - ff; focused (2 μm) - nf	856 mm for ff ; 7 & 8.5 mm for nf	1 layer - tomo; 2 layers - ff; 65 layers, 5 um step - nf
0.1 dpa/450°C	88.003	1.8 × 1 - tomo; 1.8 × 0.32 - ff; focused (2 μm) - nf	856 mm for ff ; 11 & 14 mm for NF	1 layer - tomo; 2 layers - ff; 129 layers, 5 um step - nf
0.1 dpa/300°C	88.003	1.8 × 1 - tomo; 1.8 × 0.32 - ff; focused (2 μm) - nf	856 mm for ff ; 11 & 14 mm for NF	1 layer - tomo; 2 layers - ff; 129 layers, 5 um step - nf

Grain reconstruction was performed using the Microstructural Imaging using Diffraction Analysis Software (MIDAS). Figure 4 shows an example of the reconstructed grain maps in real space of the same area measured by nf- and ff-HEDM in the unirradiated Fe-9Cr specimen. Figures 4 (a) and (b) show ff-HEDM data, in which grains are represented by spheres showing the center-of-mass (the centroid of the sphere) and the volume (the size of the sphere) of the grain. The colors indicate the completeness in Fig. 4(a) and the strain ($\times 10^{-6}$) in Fig. 4(b). The completeness is a measure of the reconstruction confidence, ranging from 0 to 1, calculated by the number of matched diffraction spots divided by the number of expected diffraction spots. Figures 4 (c) and (d) are nf-HEDM results showing the actual shapes of the grains. The colors in Fig. 4(c) show the completeness and in Fig. 4(d) show one of the Euler angles (Euler 0) of the grains with respective to the specimen coordination system. The ff-HEDM provides accurate measurements of microstrains due to its high angular resolution, while nf-HEDM can reveal the shapes of the grains due to its high spatial resolution.

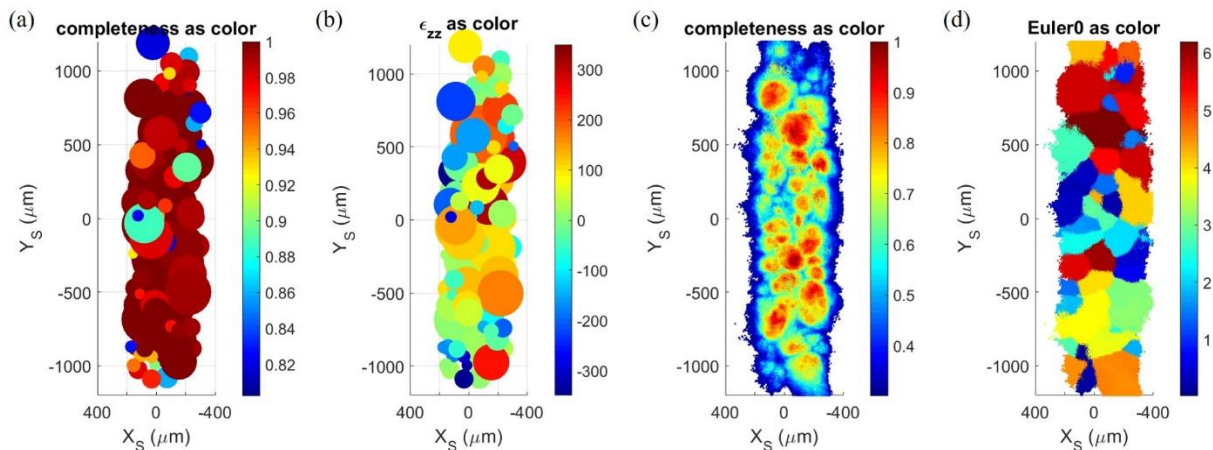


Figure 4. Reconstructed grain maps in real space of the same area measured by nf- and ff-HEDM in the unirradiated Fe-9Cr specimen (a) and (b) ff-HEDM measurement, (c) and (d) nf-HEDM measurement.

Far-field HEDM results of neutron-irradiated Fe-9Cr alloy

Figure 5 shows the ff-HEDM reconstruction data for the unirradiated Fe-9Cr specimen in real space and in the Rodrigues-Frank (RF) orientation space. Two layers measured by ff-HEDM were reconstructed individually, and grains that were artificially sliced were stitched together. The stitching algorithm was based on the misorientation angle, and a thresholding angle of 2° was used

in the analysis. The same threshold angle was used for grain identification in the nf-HEDM data analysis. Sixty-one grains were found in the measured volume in the unirradiated specimen. The average grain radius was $158\ \mu\text{m}$. Four largest grains identified were labeled as 1 to 4 in the top view (middle) in real space and in the RF orientation map (right) in Fig.5. Those four grains were used as fiducials for correlating the ff-HEDM and nf-HEDM results, and were tracked by ff-HEDM during the subsequent *in situ* tensile test.

Figures 6 and 7 show the ff-HEDM reconstruction of the $450^\circ\text{C}/0.1\text{dpa}$ specimen and the $300^\circ\text{C}/0.1\text{dpa}$ specimen, respectively. The average grain radius of the $450^\circ\text{C}/0.1\text{dpa}$ specimen was $166\ \mu\text{m}$ and $134\ \mu\text{m}$ for the $300^\circ\text{C}/0.1\text{dpa}$ specimen. Similar to the unirradiated specimen, four grains were selected in each of the irradiated specimens for comparison with nf-HEDM results and also serving as fiducials during the *in situ* tensile tests.

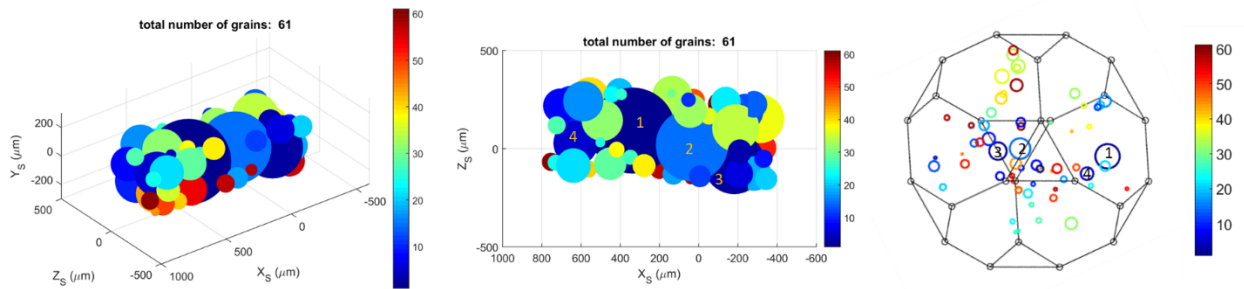


Figure 5. ff-HEDM reconstruction of unirradiated Fe-9Cr: (left) 3D view and (middle) top view in real space; (right) RF orientation space view. The selected four grains are labeled as 1 to 4 in the top view and the orientation space view.

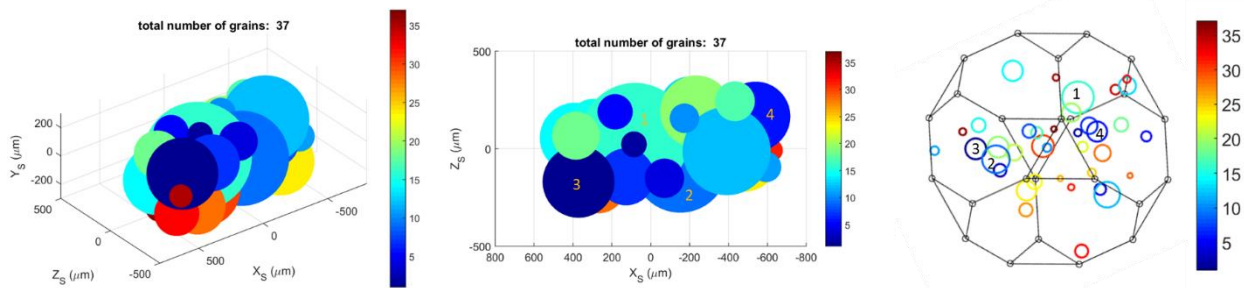


Figure 6. ff-HEDM reconstruction of $450^\circ\text{C}/0.1\text{dpa}$ irradiated Fe-9Cr: (left) 3D view and (middle) top view in real space; (right) RF orientation space view.

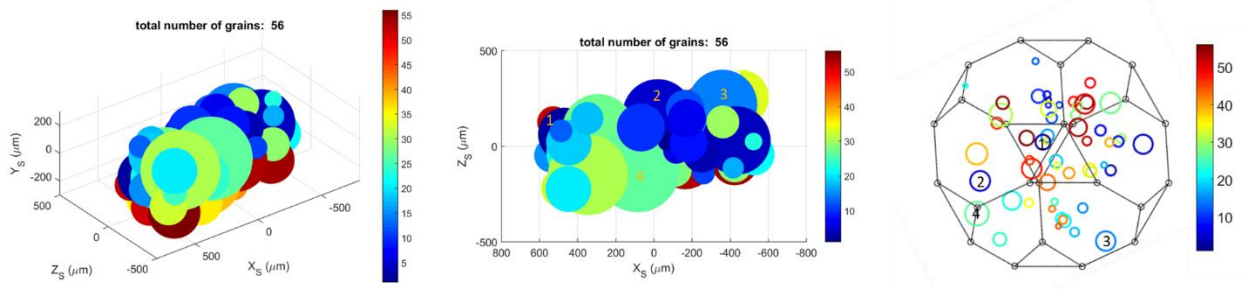


Figure 7. ff-HEDM reconstruction of $300^\circ\text{C}/0.1\text{dpa}$ irradiated Fe-9Cr: (left) 3D view and (middle) top view in real space; (right) RF orientation space view.

Near-field HEDM results of neutron-irradiated Fe-9Cr alloy

Figure 8 shows the nf-HEDM reconstruction of the middle layers of the unirradiated, and irradiated 450°C/0.1 dpa and 300°C/0.1 dpa specimens of the Fe-9Cr alloy. The grain maps are represented in three color bars: completeness, one of the Euler angle component (Euler0), and the kernel average misorientation (KAM). Out of those three, the completeness and the Euler0 plots are visualization of the direct output from the MIDAS software. The pixels in the KAM plots are the averages of the misorientation angles calculated using a given pixel and its first and second nearest neighbors. The KAM values are sensitive to local orientation changes, and are plotted to highlight the locations of boundaries where there are orientation discontinuities (e.g. grain boundaries, subgrain boundaries). As shown in each of the KAM plots in Fig. 8, the red lines outline the high angle grain boundaries in each specimen.

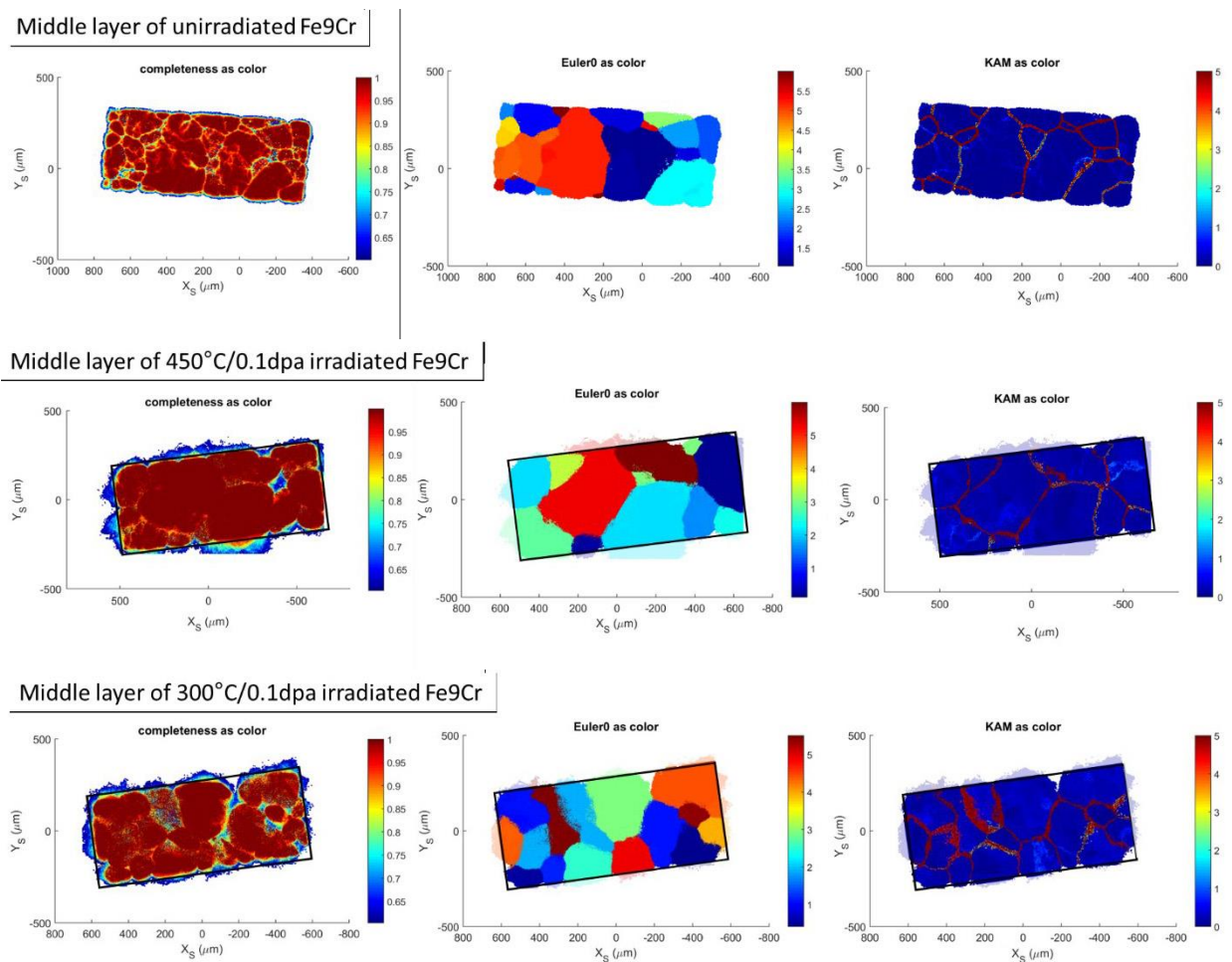


Figure 8. Nf-HEDM reconstruction of the middle layers of the three specimens: layer 33 for the unirradiated, layer 65 for the 450°C/0.1dpa irradiated and for the 300°C/0.1dpa irradiated. Color bars indicate completeness (left), Euler0 angle (middle), and KAM (right).

Grains were identified based on orientations using the same stitching algorithm as in the ff-HEDM. The grain identification algorithm also used 2° as the misorientation threshold angle in the nf-HEDM data analysis. Pixels with misorientations equal to and smaller than the threshold value were considered as one grain. Since there are 300k -500k pixels in each layer and the pairwise misorientation calculation is computationally costly, the grain identification algorithm was performed on randomly-selected 5000 pixels in the first step. In the second step, the average orientation of the grain identified in the first step was calculated. Those grain orientations were plotted in the RF orientation space together with the orientations from all the pixels to visually confirm that all the orientations in the microstructure were sampled. In the last step, the misorientations between all the pixels and those averaged grain orientations were calculated, and the 2° threshold was used to group pixels with almost the same orientations as one grain. Figure 9 shows the grain identification result in real space and in orientation space. Color bars indicate grain IDs. Four largest grains identified in the ff-HEDM were also found by nf-HEDM, and labeled as 1 to 4 in each specimen in Fig. 9.

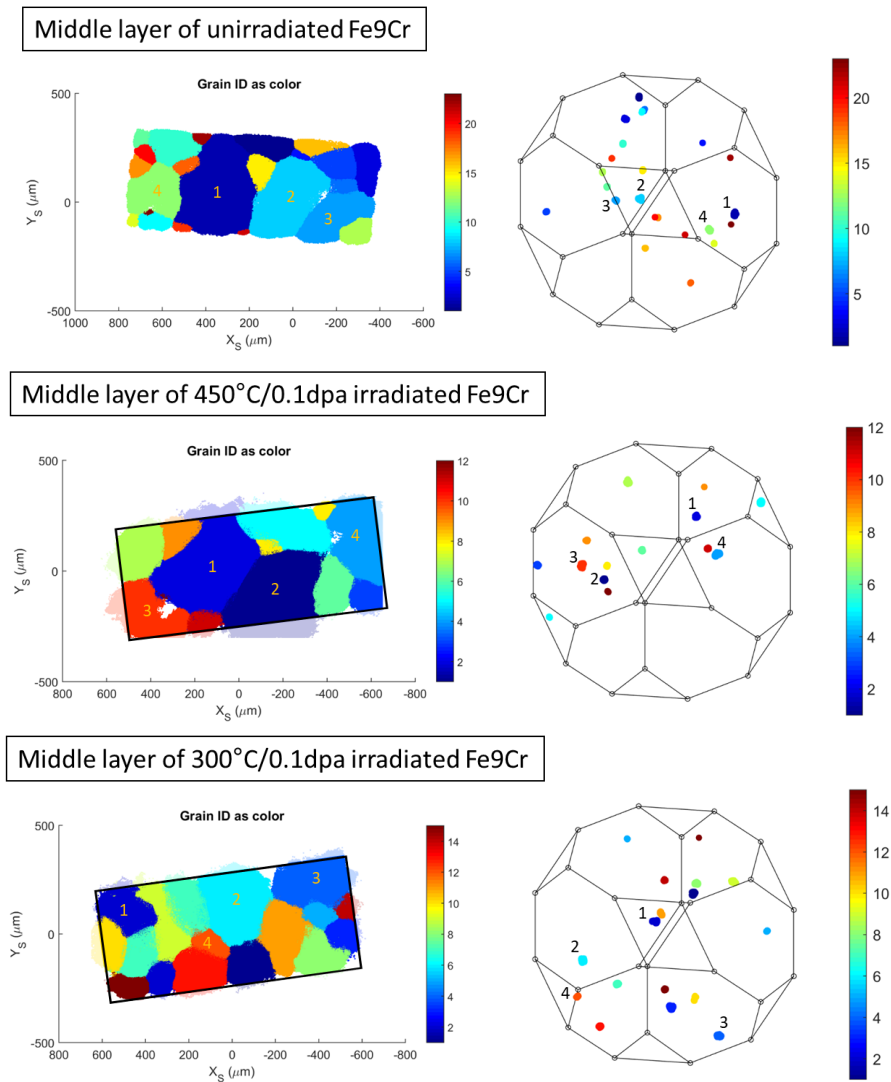


Figure 9. Nf-HEDM reconstructions of the middle layers of the three specimens: the unirradiated, the $450^\circ\text{C}/0.1\text{dpa}$ irradiated and the $300^\circ\text{C}/0.1\text{dpa}$ irradiated. Colors indicate the grain IDs.

With 65 layers measured for the unirradiated specimen and 129 layers measured for each of the irradiated specimens at the 5 μm step along the gage length direction, mm^3 -sized volumes were documented for their grain structures, including grain locations, shapes, and orientations. Figure 10 shows the 3D reconstructions of the high-angle grain boundaries in the three specimens. Only pixels with KAM $> 5^\circ$ were plotted.

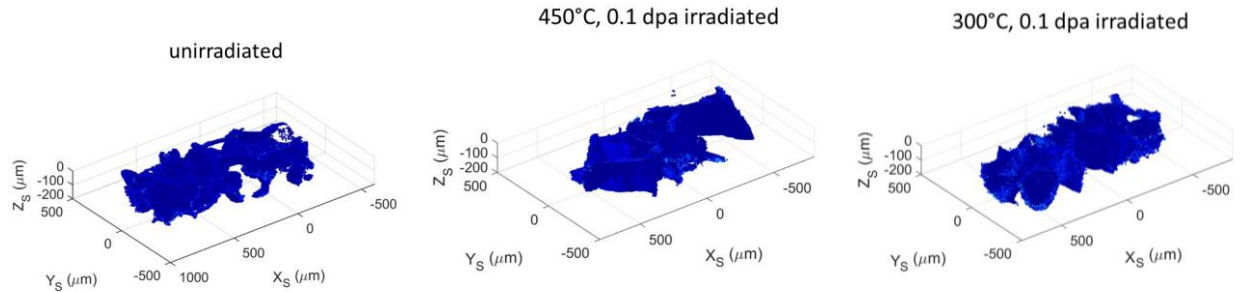


Figure 10. 3D high-angle grain boundary maps obtained from nf-HEDM of the three specimens: the unirradiated, the 450°C/0.1dpa irradiated and the 300°C/0.1dpa irradiated.

2.2.2. *In situ* tensile test with far-field HEDM and WAXS of Neutron-Irradiated Fe-9Cr Alloy

Experimental Procedure

In situ tensile tests were conducted using the Psylotech micro test system at the APS beamline 1-ID on the above three specimens: unirradiated, and neutron-irradiated to 0.1 dpa at 300 and 450°C, respectively, of the Fe-9Cr alloy. The experimental setup at the beamline is shown in Fig. 11. The irradiated specimen was contained in a double-layered Kapton tube integrated with the tensile gripping device. In addition, a plastic housing was used to cover the entire load frame, serving as the secondary containment of the irradiated specimen. The micro test system was mounted on a kohzu motorized precision positioning stage. A single GE-RT41 area detector, centered relative to the direct beam, was located nominally 881 mm downstream from the specimen to collect diffraction signals. For ff-HEDM, outer diffraction rings are desired since they give higher angular resolution. To maximize the outer ring intensities without supersaturating the inner rings, a circular lead shield was attached to the surface of the detector covering the inner two rings ($\{110\}$ and $\{200\}$) to reduce their diffraction intensities, as shown in Fig. 11.

The *in situ* tensile tests were conducted at room temperature in displacement control at a nominal strain rate of 0.00002/sec. During the tensile test, WAXS measurement was conducted in a continuous mode, while ff-HEDM was carried out at several load levels in an interrupted mode. The X-ray energy was 81 keV. The beam size for WAXS was 0.3 mm \times 0.3 mm and the exposure time was 0.3 s. Since the specimen initially had very large grains, the specimen was rotated from -20° to $+20^\circ$ so that more grains were diffracted in the illuminated volume to obtain a power-like diffraction pattern. Ten frames of diffraction patterns were taken at a given y-position. Five scans were conducted by moving the entire load frame vertically by 0.3 mm at every scan, and a new volume was illuminated and measured. After five vertical scans were completed, the load frame was moved to the starting y-position for the next measurement. Each measurement contained a total of 50 frames of diffraction patterns that were summed during the analysis of the WAXS data,

which gives the strain resolution of 0.25% in the plastic deformation regime. The signals covering $\pm 15^\circ$ around the loading axis was integrated into 1D diffraction profiles for peak fitting to obtain lattice spacings. The signals from the entire diffraction ring was caked into 10° slices, integrated individually into 1D profiles, fitted individually to obtain peak intensities and peak full width at half maximum (FWHM). Those FWHM values were weight-averaged by the peak intensities to obtain the FWHM for the entire ring. The modified Williamson-Hall method was used to estimate the dislocation density and the coherently diffracting domain size from the FWHM data.

Far-field-HEDM measurements were performed at intermittent loading points. Before each ff-HEDM measurement, the tensile load was reduced to the pre-loading level (25 MPa) at a given strain level, and ff-HEDM measurement was performed in the nominally “unloaded” state. The beam size for ff-HEDM was $1.7 \text{ mm} \times 0.3 \text{ mm}$. The specimen was rotated continuously from -180° to $+180^\circ$, and one diffraction image was taken at every 0.25° interval. When one rotation was completed, the load frame moved vertically by 0.3 mm and another scan was carried out in the same fashion. Five continuous layers were measured in total with the middle layer at the center of the specimen gauge. After all 5 scans were finished, tensile loading resumed. Due to the presence of the two posts of the load frame, X-ray beams in certain rotation angles were blocked. For ff-HEDM reconstruction, only signals from -180° to -110° , -70° to 70° , and 110° to 180° were used. The third to the eighth rings of the bcc phase, $\{211\}$, $\{220\}$, $\{310\}$, $\{222\}$, $\{321\}$, $\{400\}$, were used for reconstruction. The stitching algorithm was applied to recover grains that were sliced into different layers. When subgrains formed under tensile deformation, parent grains were recovered by setting an appropriate threshold angle. This enables tracking of the deformation process of individual grains during tensile deformation. Due to the limited distance allowed between the specimen and the nf-HEDM detector (a few millimeters), the tensile test set-up designed for radioactive specimens made it impossible to conduct nf-HEDM *in situ*. Nf-HEDM measurements can be carried out before and after an *in situ* tensile test to capture the beginning and end states of tensile deformation, which is described in Section 2.3.3.

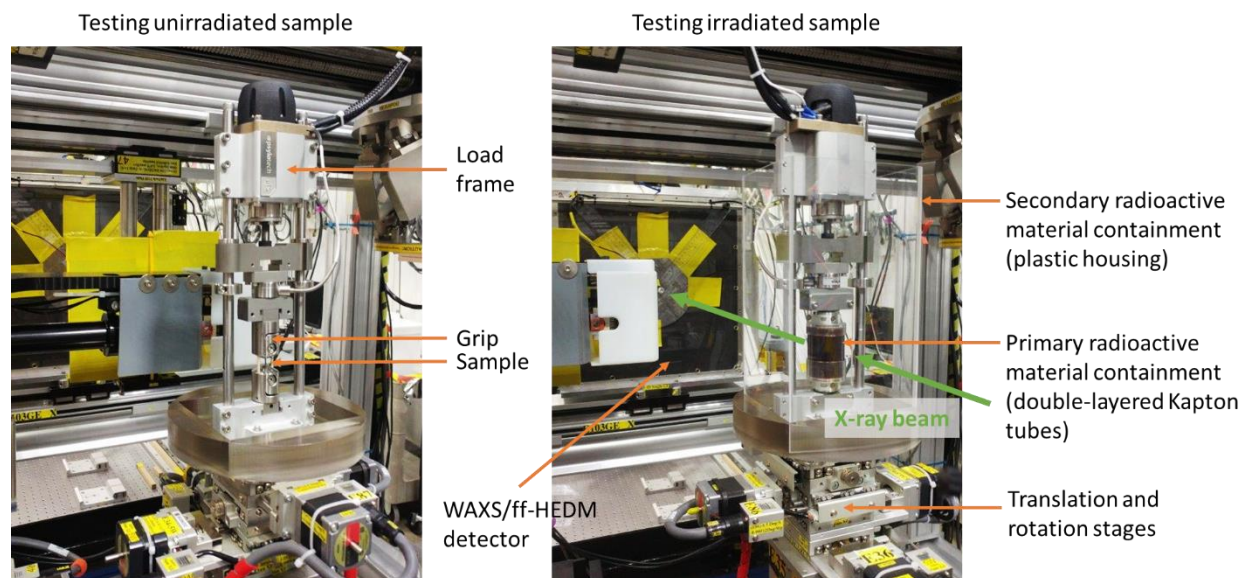


Figure 11. Experimental setup for *in situ* tensile test of an unirradiated (left) and a neutron-irradiated (right) Fe-9Cr specimens at the APS beamline 1-ID.

Engineering Stress-Strain Curves

Figure 12 shows the stress-strain curves of the *in situ* tensile tests of the unirradiated and 450°C/0.1dpa irradiated Fe-9Cr specimens. Colors indicate different loading segments where WAXS measurements were taken continuously and HEDM measurements were taken at the beginning and end of the segment. The dashed lines schematically show the re-loading curves after an HEDM measurement was completed. The tensile tests were intentionally ended at the given strain levels where diffraction ring patterns were observed and HEDM data analysis became challenging. The tensile-deformed specimens were preserved for post-mortem *ex situ* nf- and ff-HEDM measurements. Figure 12 shows that neutron irradiation to 0.1 dpa at 450°C significantly increased the yield stress (from 130 to 290 MPa), but had an insignificant effect on work hardening in the early stage of tensile deformation of the Fe-9Cr alloy.

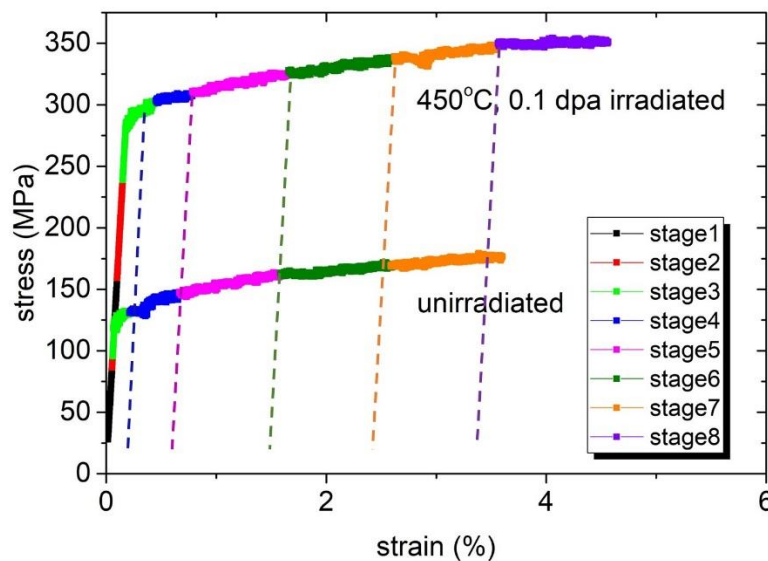


Figure 12. Stress-strain curves of the unirradiated and the irradiated Fe9Cr specimens obtained from the in-situ tensile tests.

Results of ff-HEDM

Figure 13 shows the grain maps in the unirradiated specimen before and after deformation to 2.6% strain in the real space as well as in the orientation space. The color bar shows the numbers of grains measured by ff-HEDM. A threshold angle of 2° was used in the stitching algorithm. As shown in Fig. 13, comparable numbers of grains were found, 155 for the undeformed and 174 for the 2.6% deformed states. The orientation plot revealed remarkable similarities between the two states. Similar observations were made in the 450°C/0.1dpa irradiated specimen as shown in Fig. 14. The number of grains found in the undeformed state was 86, and 81 in the 2.6% deformed state in the 450°C/0.1dpa irradiated specimen. These results indicate that ff-HEDM successfully tracked the same group of grains in both specimens during tensile deformation.

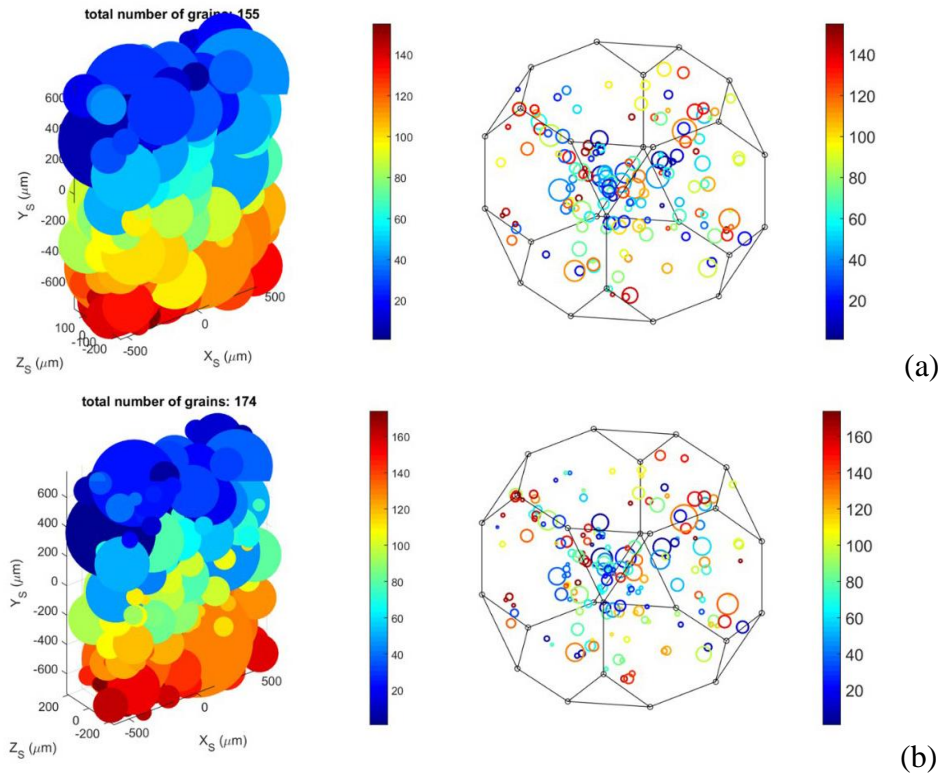


Figure 13. Far field-HEDM reconstruction of the unirradiated specimen in the real space and the orientation space. (a) The undeformed state, and (b) the 2.6% deformed state. Color bars indicate the numbers of grains.

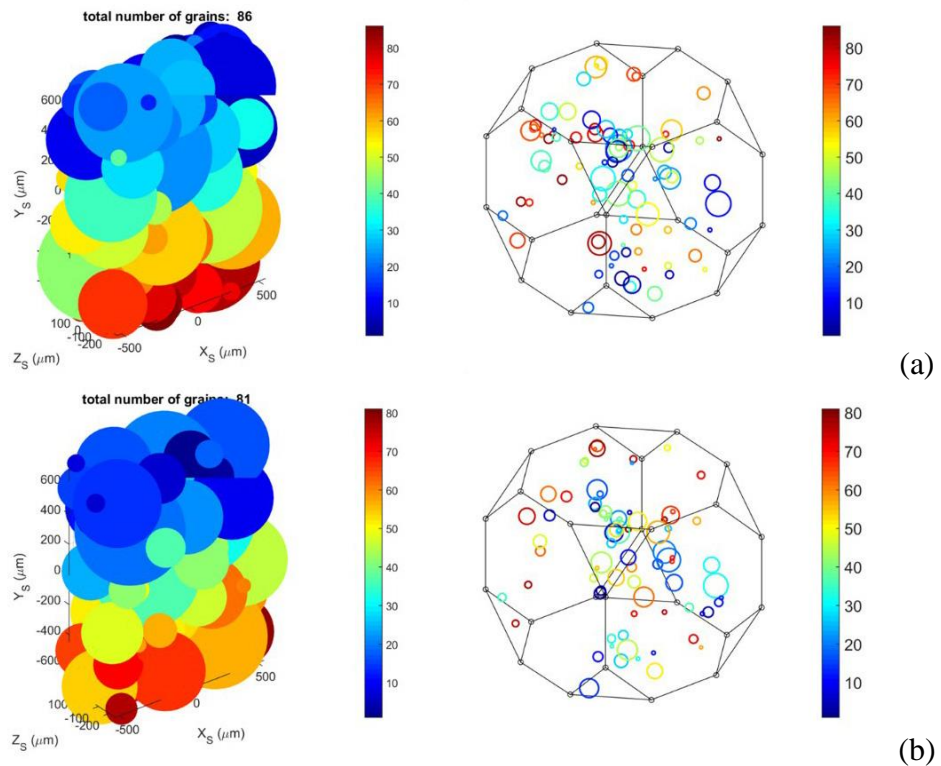


Figure 14. Far field-HEDM reconstruction of the 450°C/0.1dpa irradiated specimen in the real space and the orientation space. (a) The undeformed state; (b) the 2.6% deformed state. Color bars indicate the numbers of grains.

To follow the evolution of individual grains during tensile deformation, grain IDs were assigned to a group of grains with the radius larger than $100\ \mu\text{m}$ (the grain radius was arbitrarily selected). The misorientations between the grains from the undeformed and the deformed states were calculated, and the grains with misorientation angles smaller than 3° were paired. For the unirradiated specimen, 43 grains were selected and assigned unique IDs. Figure 15 plots those 43 grains in the real space and in the orientation space before and after the 2.6% tensile deformation. Grain structure appears remarkably similar between the undeformed and deformed states. For the $450^\circ\text{C}/0.1\ \text{dpa}$ irradiated specimen, one layer of grains had to be discarded due to an unintentional offset ($300\ \mu\text{m}$) between the measured volumes of the undeformed and 2.6% deformed states, and only four layers were analyzed. Twenty-three grains were assigned unique IDs, as shown in Fig. 15.

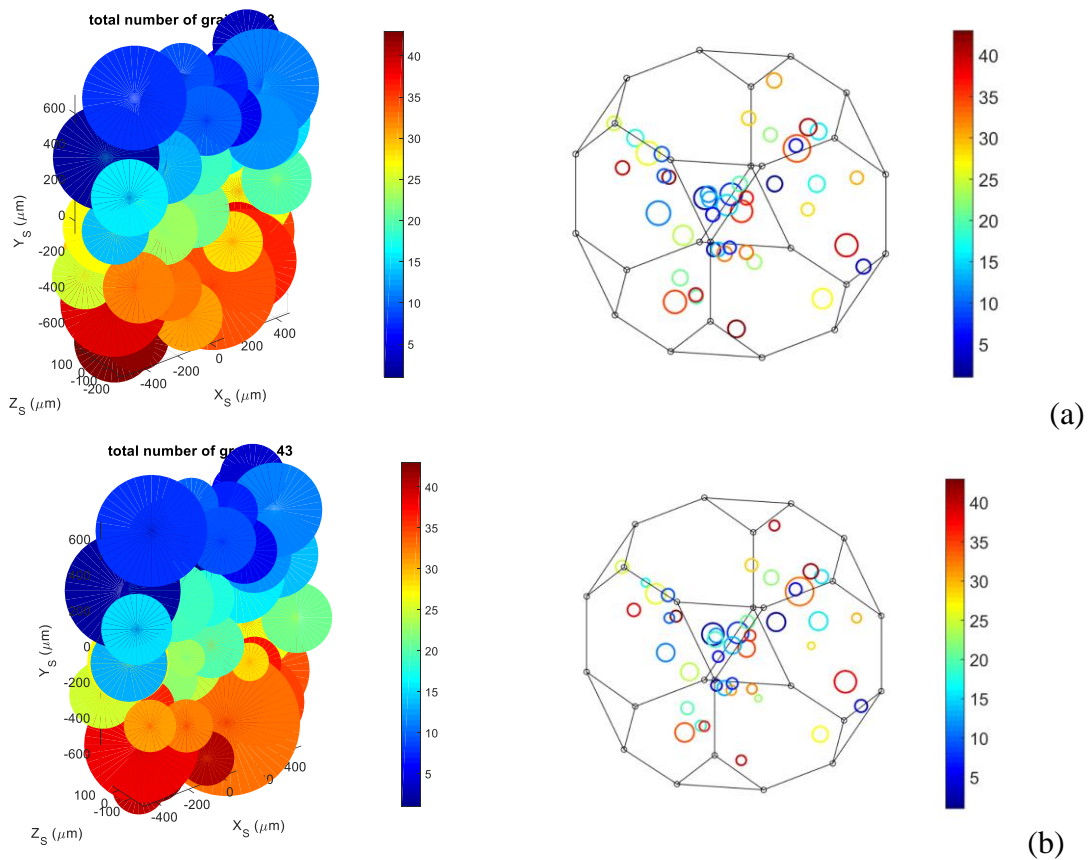


Figure 15. Far field-HEDM reconstruction of 43 selected grains in the unirradiated specimen in the real space and the orientation space: (a) the undeformed state; (b) the 2.6% deformed state. Color bars indicate grain IDs.

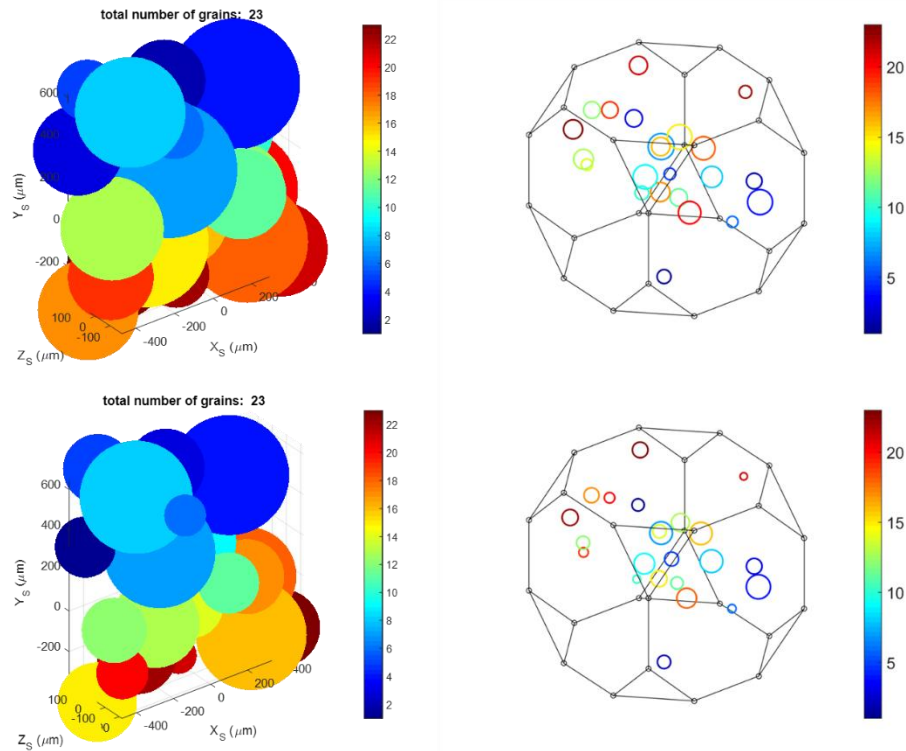


Figure 16. Far field-HEDM reconstruction of 23 selected grains in the 450°C/0.1dpa irradiated specimen in the real space and the orientation space: (a) the undeformed state; (b) the 2.6% deformed state. Color bars indicate grain IDs.

Diffraction spots for each individual grain were extracted and fitted with 2D Gaussian function to obtain peak broadening in the azimuthal and the radial directions. Figure 17 shows one diffraction spot from the $\{211\}$ reflections of a grain in the unirradiated Fe-9Cr specimen before and after 2.6% deformation. The full detector image of the 2.6% deformation state at the particular rotation angle where the spot (circled in red) is most bright is also shown. Information of peak broadening was used to study the effect of irradiation and deformation in the Fe-9Cr alloy. It is seen that the diffraction spot broadens in both the radial direction (r) and the azimuthal direction (azi) due to deformation. The broadening in the azimuthal direction is a measure of the orientation changes within grain interiors, and the broadening in the radial direction is a measure of the long-range strain and sub-domain size within grains. The broadening data were quantified by fitting the spot with a 2D Gaussian function. The histograms of the broadening data from 43 grains in the unirradiated specimen before and after deformation are shown in Fig. 18, where Fig. 18 (a) shows the broadening in the azimuthal direction and Fig. 18 (b) shows the broadening in the radial direction. Data from each $\{hkl\}$ used for ff-HEDM reconstruction is plotted separately. The differences between $\{hkl\}$ s are insignificant in either the radial direction or the azimuthal direction, and thus the data of multiple $\{hkl\}$ reflections in each direction were combined and plotted in Fig. 19 for the unirradiated specimen, and in Fig. 20 for the 450°C/0.1 dpa specimen (23 grains in total). It is noted that significant broadening was observed in both azimuthal and radial directions after 2.6% deformation. Even at this early deformation stage, the grain interior developed noticeable orientation spread, and the internal strain increased considerably due to a rapid increase of dislocation density.

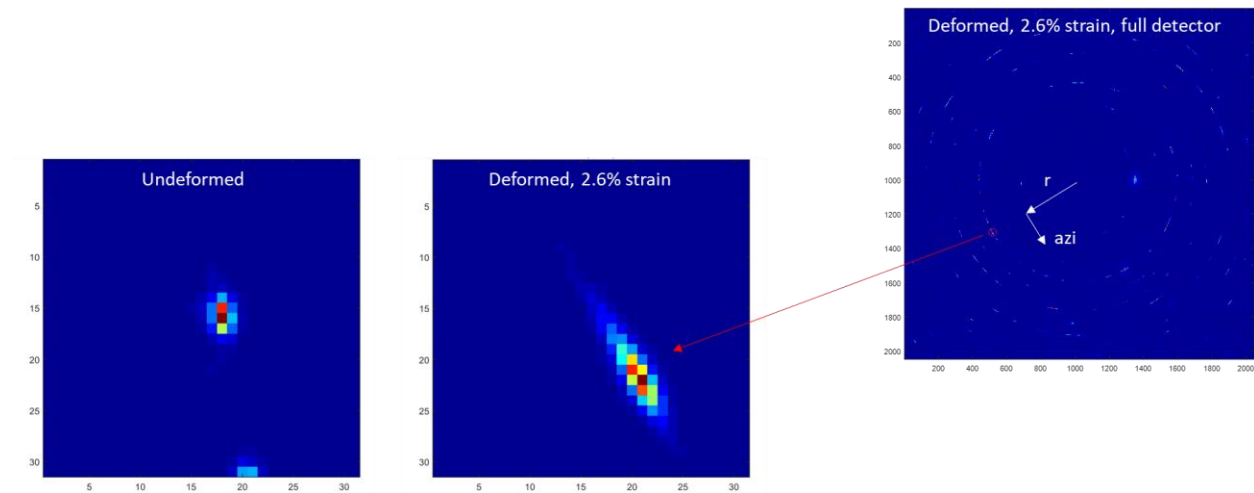


Figure 17. Images of the diffraction spot before and after deformation. The spot is taken from the {211} ring of a grain in the unirradiated specimen.

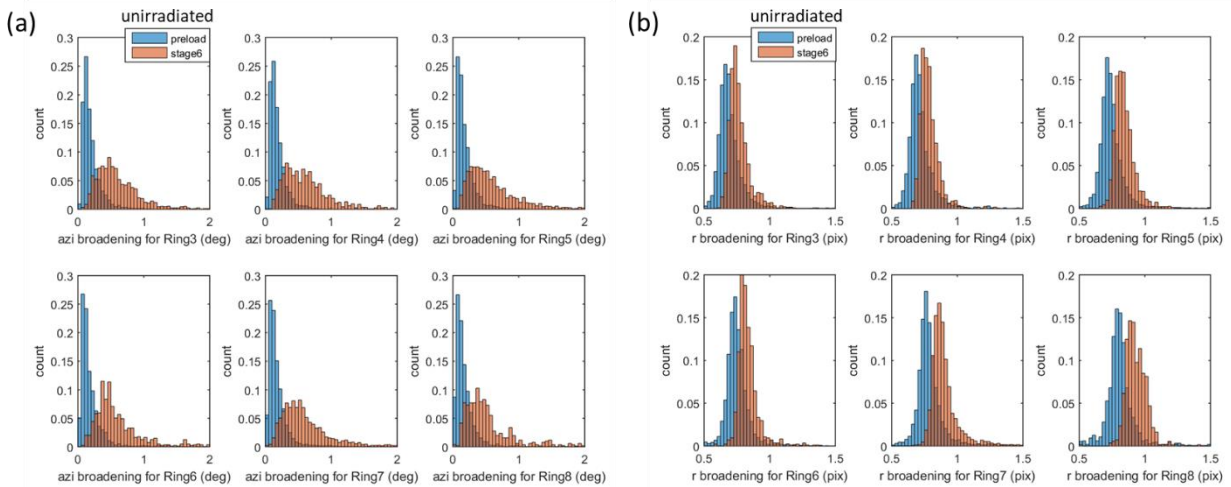


Figure 18. Peak broadening in the unirradiated specimen for individual {hkl} rings before and after 2.6% deformation. (a) In the azimuthal direction; (b) in the radial direction.

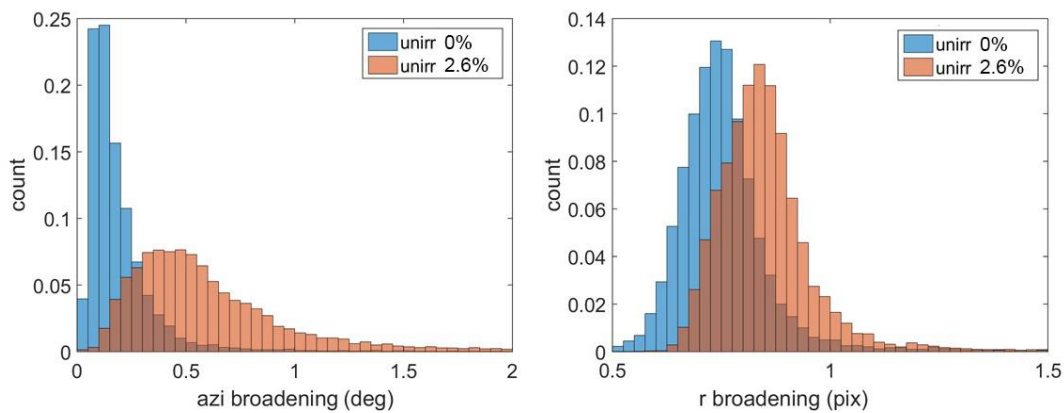


Figure 19. Peak broadening in the unirradiated specimen averaged over all {hkl} rings of the 43 selected grains before and after 2.6% deformation: (Left) in the azimuthal direction; (Right) in the radial direction.

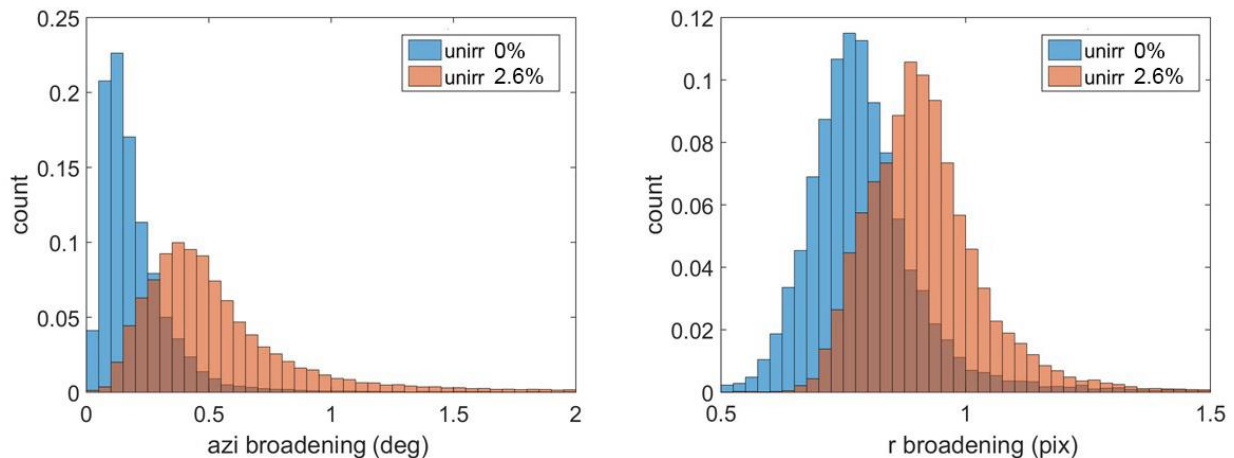


Figure 20. Peak broadening in the 450°C/0.1 dpa irradiated specimen averaged over all {hkl} rings from the 23 selected grains before and after 2.6% deformation: (Left) in the azimuthal direction; (Right) in the radial direction.

The effect of irradiation and deformation in the Fe-9Cr alloy is better revealed in Fig. 21 where the histograms in Figs. 19 and 20 were combined. In the azimuthal direction, the effect of irradiation is not obvious. The broadening profiles in the undeformed states of the unirradiated and irradiated specimens are nearly the same. The broadening profiles in the deformed states of the two specimens are also similar, with a slight intensity difference. In the radial direction, the effect of irradiation is more pronounced. At the early stage of deformation (2.6% strain), radiation-induced dislocation loops and deformation-induced dislocation lines are the main sources of the radial broadening. In the undeformed state, the radial broadening in the irradiated specimen was more pronounced than that in the unirradiated specimen, indicating that irradiation-induced dislocation loops contribute to the radial broadening. After deformation, the difference in broadening became stronger, likely due to the generation of high-density dislocations.

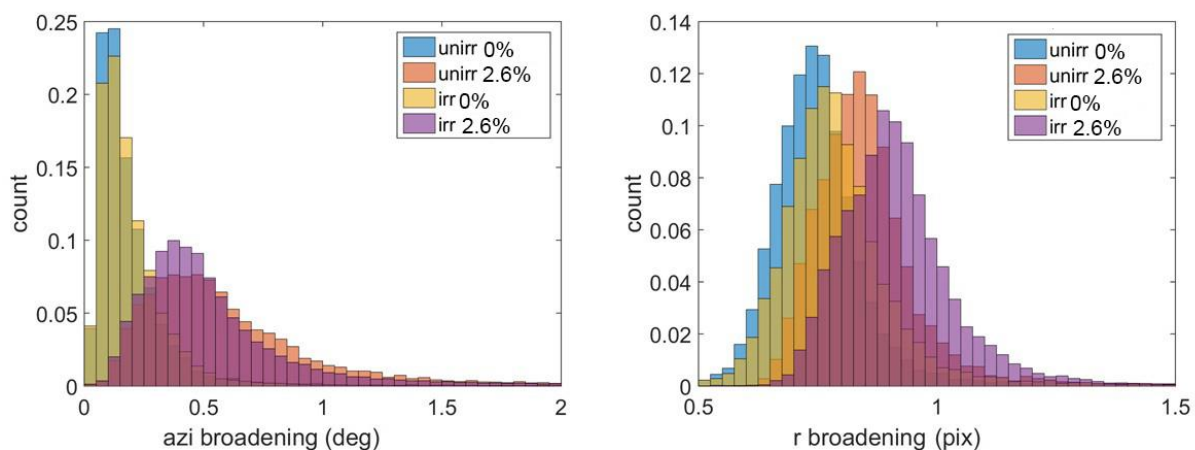


Figure 21. Peak broadening in the unirradiated and 450°C/0.1 dpa irradiated specimens before and after 2.6% deformation: (Left) in the azimuthal direction; (Right) in the radial direction.

2.2.3. *Ex situ near- and far- field HEDM and Tomography of Neutron-Irradiated Fe-9Cr Alloy after in situ Tensile Test*

Fe-9Cr specimens were also characterized by nf- and ff-HEDM and tomography after *in situ* tensile tests at the APS beamline 1-ID. This section summarizes *ex situ* HEDM measurements of tensile-deformed unirradiated and irradiated (450°C/0.01 dpa) specimens. Both specimens were tensile tested until necking occurred. HEDM measurements were conducted in the grip section representing the undeformed state and in the uniformly-deformed area of the gauge section representing the deformation state at the uniform elongation, as shown in Fig. 22. The beam energy was 88 keV and the beam size was 2 mm × 1 μm (focused) for both nf- and ff-HEDM. The far-field deflector was 994 mm downstream from the specimen, and the near-field detector was at 11-17 mm from the specimen. During a scan, the specimen rotated from -180° to 180° continuously and the detectors recorded diffraction images at 0.25° intervals. Up to 25 layers were measured in the undeformed areas with a step size of 20 μm along the specimen length direction, and one layer was measured in the deformed area. The same volume of each layer was measured by both nf-HEDM and ff-HEDM.

Grain reconstruction was performed using the Microstructural Imaging using Diffraction Analysis Software (MIDAS). For ff-HEDM, MIDAS calculates the properties of diffraction spots and assigned (indexed) the diffraction spots to grains, and then calculated the properties of grains. For nf-HEDM reconstruction, a simulation grid consisting of elementary triangles with an edge length of 3 μm was created for the measured layer of the specimen. The diffraction signals at each point (voxel) were calculated and compared with the experimental data for best match. The ff-HEDM reconstruction was performed first, and the results were used as seeds for nf-HEDM reconstruction to speed up the computationally intensive analysis by limiting the search space. For the undeformed areas the ff-HEDM reconstruction used the 1st to 7th rings of the ferrite phase ({110}, {200}, {211}, {220}, {310}, {222}, {321}) and a completeness threshold of 0.8. For the deformed areas, the ff-HEDM reconstruction used the 2nd to 5th rings of the ferrite phase ({200}, {211}, {220}, {310}) and a completeness threshold of 0.5.

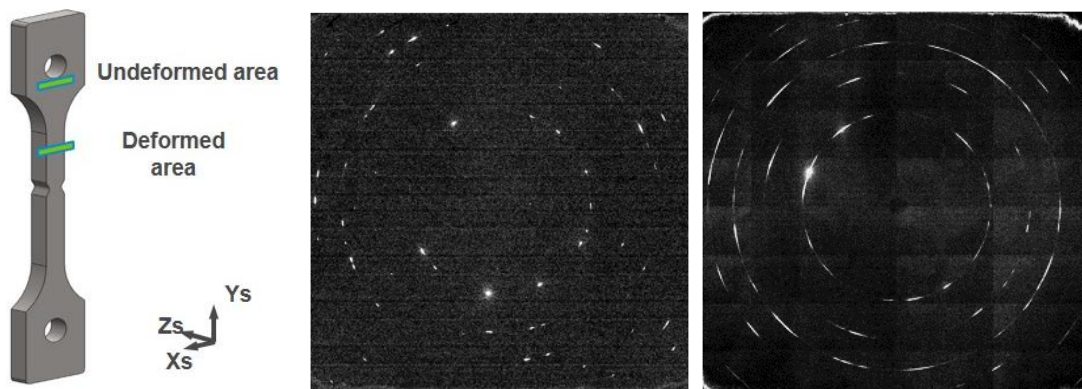


Figure 22. (Left) Tensile deformed specimen, (middle) diffraction pattern of the undeformed area, and (right) diffraction of the uniformly-deformed area.

Figure 23 shows the nf-HEDM reconstruction results of the undeformed and deformed regions in the unirradiated and 450°C/0.01 dpa irradiated specimens, respectively. Only one layer

of the specimen is shown in Fig. 23. Color represents the Kernel Averaged Misorientation (KAM). The KAM of each pixel is calculated as the average of the misorientation angles between a given pixel and its first and second nearest neighbors. The color scale in Fig. 23 is 0 - 5, and the red color outlines high angle grain boundaries. It is seen that both the unirradiated and irradiated specimens show minimal orientation changes in grain interiors before tensile tests. After tensile deformation, grain interiors have dramatic orientation changes, and grains split into subgrains.

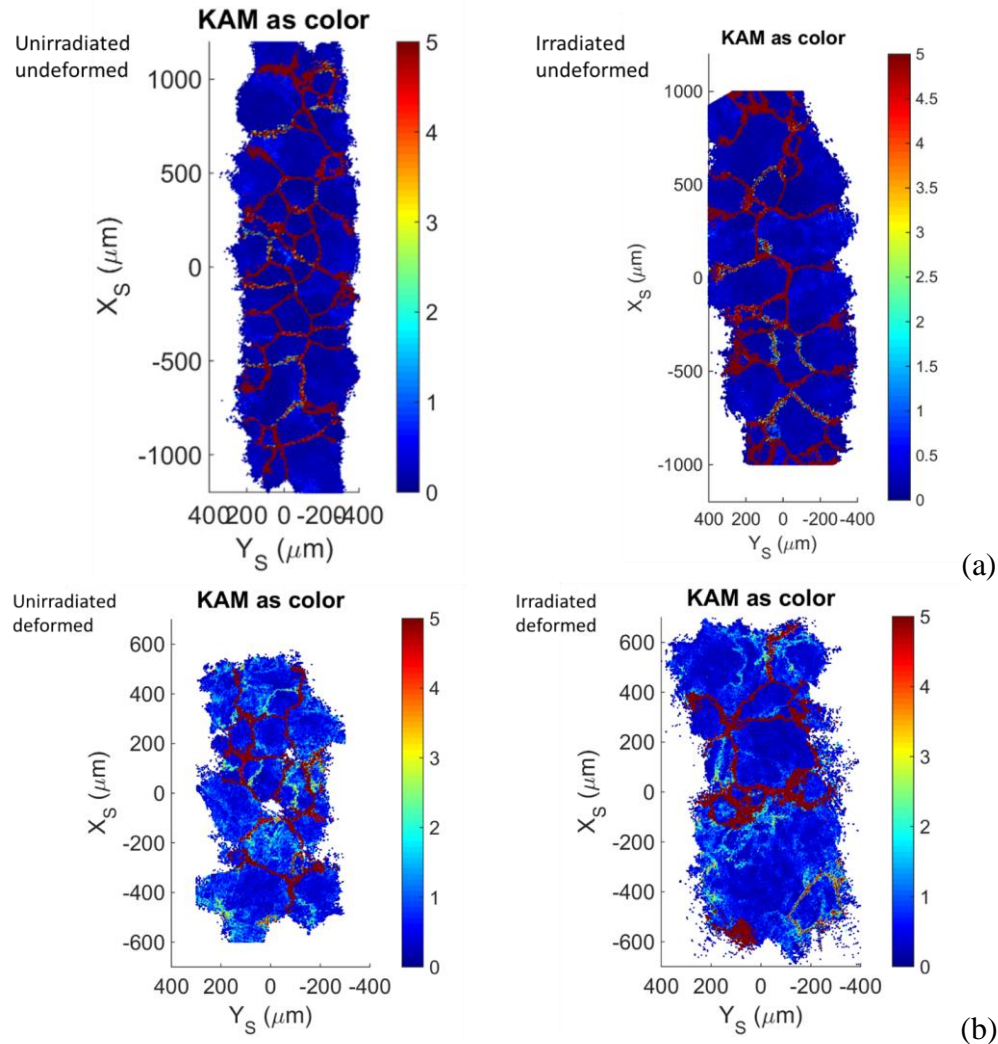


Figure 23. KAM maps from nf-HEDM measurements of the undeformed and deformed regions in the (a) unirradiated and (b) 450°C/0.01 dpa irradiated specimens.

In order to obtain information of individual grains, an orientation-based clustering algorithm was applied to the MIDAS output to index each grain. A misorientation angle threshold of 1° for the undeformed areas and 3° for the deformed areas was applied to both ff-HEDM and nf-HEDM data. Elements with misorientation angles smaller than the threshold were grouped into one grain, and assigned a unique ID (“Element” is a general term that refers to the coherent scattering domains in ff-HEDM and pixels in nf-HEDM). Figure 24 shows the work flow of the

analysis for the deformed area of the irradiated specimen. The first step is to perform cluster analysis using the clustering algorithm to identify grains that have elements having similar orientations in the orientation space. Color bars are grain IDs. It is seen that in the orientation space elements segregated around a particular orientation have the same color, indicating that they are successfully grouped into one parent grain. The grain ID information is then transferred to the real space. In the real space plots, elements having the same color are physically next to each other, confirming that they indeed belong to the same parent grain. Finally, a detailed study of individual grains is carried out to analyze diffraction signals.

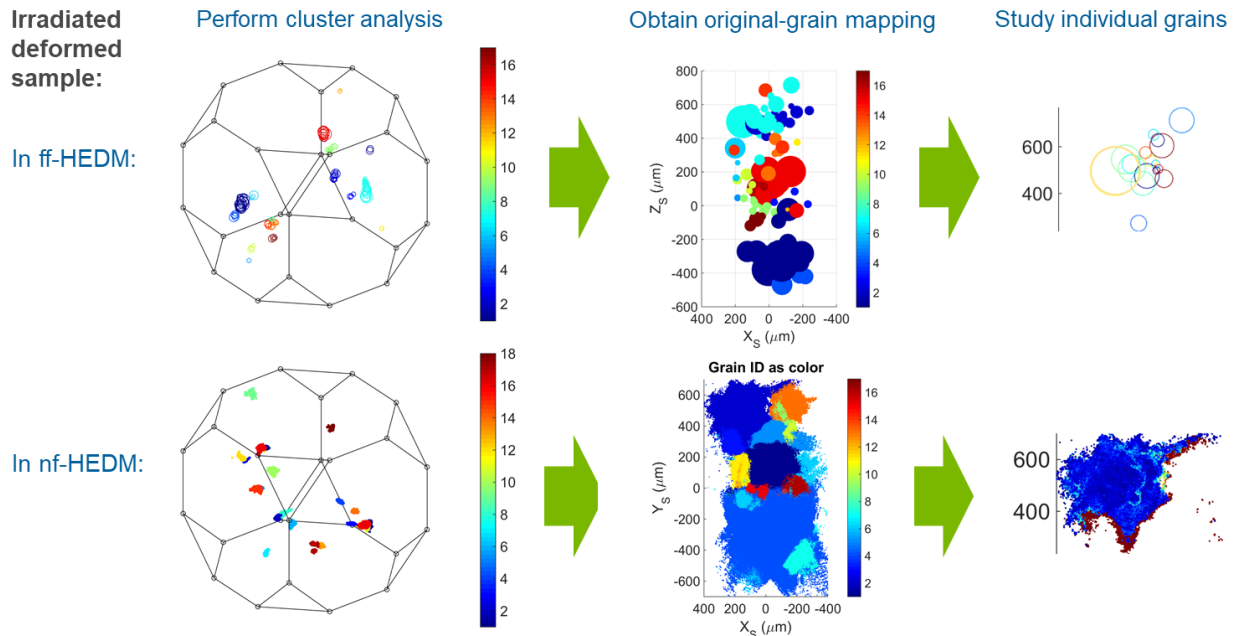


Figure 24. The work flow of grain analysis using an orientation-based clustering algorithm for the deformed area of the irradiated specimen.

Figures 25 and 26 show the HEDM data of a parent grain identified in the deformed area in the unirradiated and 450°C/0.01 dpa irradiated specimens, respectively. The Euler0 angle plots (left) and KAM plots (middle) are the results of nf-HEDM, and the ϵ_{zz} plots (right) are from ff-HEDM. Significant orientation and strain variations can be seen in deformed grains. Grain fragmentation is clearly revealed by sudden changes in orientation and the formation of subgrain boundaries. Distinctive orientation domains, i.e. subgrains are more likely to be detected by ff-HEDM due to the higher angular resolution of ff-HEDM.

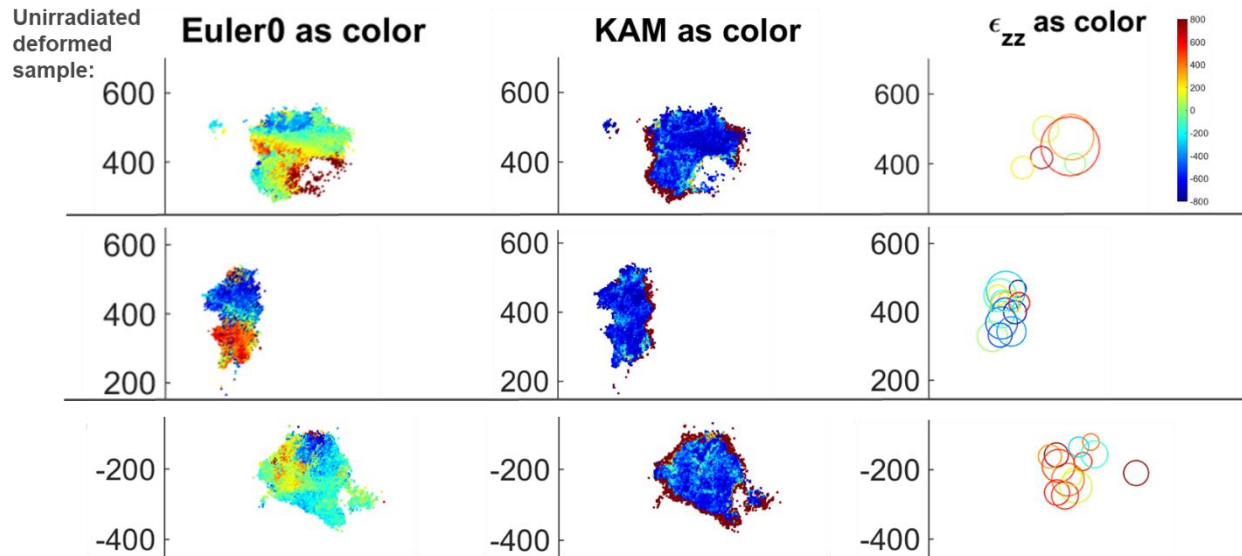


Figure 25. A parent grain identified by nf- and ff-HEDM in the deformed area in the unirradiated Fe-9Cr specimen.

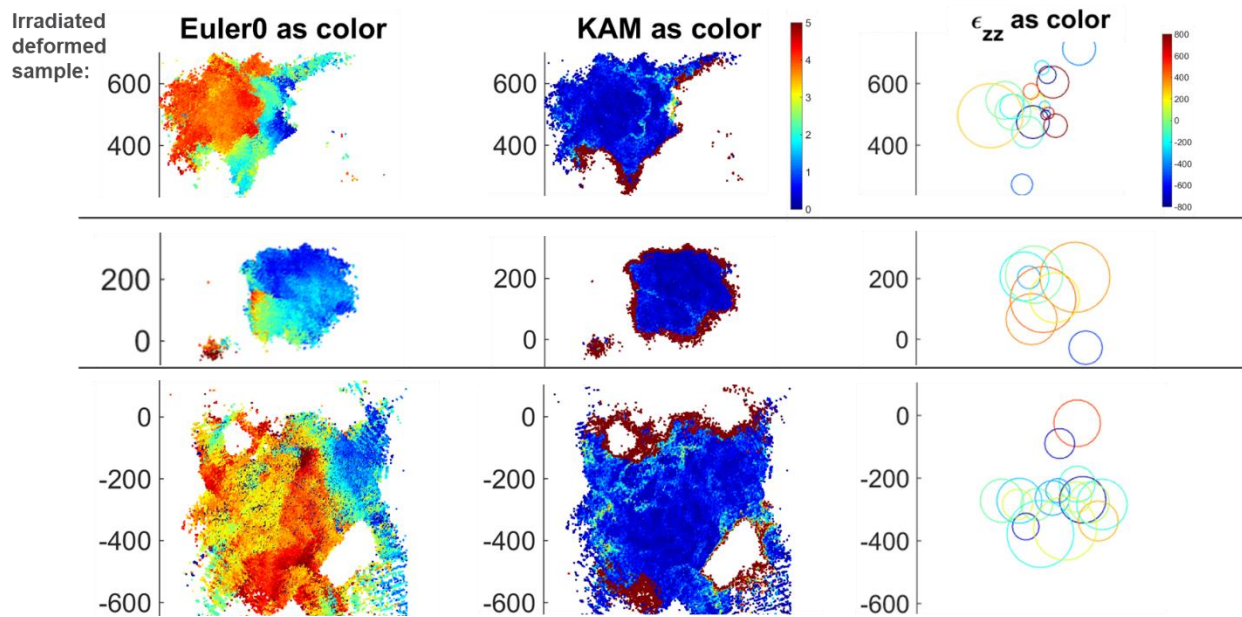


Figure 26. A parent grain identified by nf- and ff-HEDM in the deformed area in the 450°C/0.01 dpa irradiated Fe-9Cr specimen.

3 *In situ* Elevated-Temperature Tensile Tests of Neutron-Irradiated Specimens Characterized with High-Energy X-rays

The goal of this task was to demonstrate the capability for *in situ* mechanical testing of an activated specimen at elevated temperatures at the APS beamline. *In situ* tensile tests of a high-temperature, ultrafine-precipitate strengthened (HT-UPS) stainless steel were conducted at 20 and 400°C with high-energy wide-angle X-ray scattering (WAXS) and small-angle X-ray scattering (SAXS) measurements. The HT-UPS specimens were neutron irradiated to 3 dpa at 400°C at the Advanced Test Reactor. The data were published in the reference [8]. Below is a brief summary of the experiments and main results.

The *in-situ* high-energy X-ray experiments were performed at the APS 1-ID beamline. The experimental setup is described in detail in reference [9]. The specimens were subsized sheet-type tensile specimens with a nominal gauge length of 5 mm, a gauge width of 1.2 mm and a gauge thickness of 0.7-1 mm (shown in Fig. 2b). Tensile tests were performed on a MTS[®] model 858 servo-hydraulic load frame under uniaxial tension. The *in situ* **R**adioactive **M**aterials (*i*RadMat) characterization apparatus (shown in Fig. 27) [9] was used for heating as well as radiation shielding and containment for the radioactive specimens.

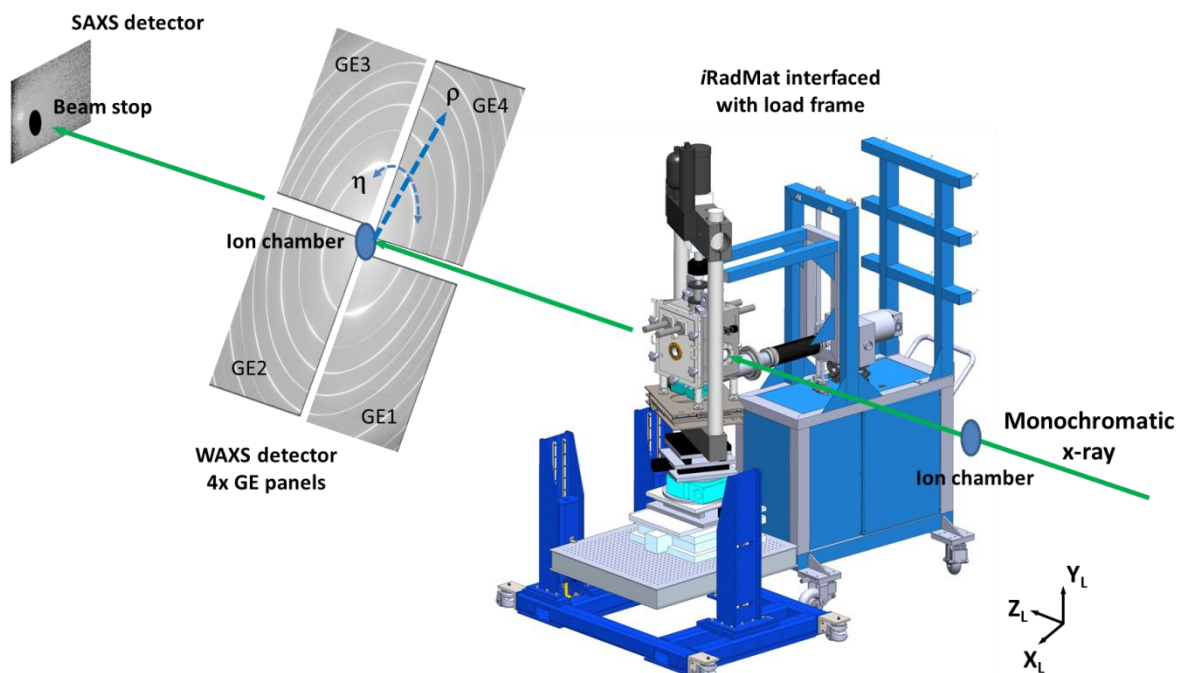


Figure 27. *In situ* WAXS/SAXS experiment set-up at beamline 1-ID featuring the iRadMat apparatus interfaced with the MTS load frame and the WAXS/SAXS detectors.

To avoid contamination of the furnace by the radioactive specimen, an encapsulation is needed between the specimen and the chamber. This encapsulation serves as the primary containment. For room temperature tests of activated specimens, two-layer Kapton tubes and 3D-printed plastic adapter pieces are used (Fig. 28(a)). For experiments at elevated temperatures and under vacuum, amorphous fused quartz tubes and stainless steel adapters are used (Fig. 28(c)) [9].

Because quartz is largely opaque to infrared wave radiation from the heaters, specimen heating is primarily carried out by conduction. An activated tensile specimen was pre-assembled into a gripping device and surveyed by Health Physics at Argonne’s radiological facility, Irradiated Materials Laboratory, prior to transfer to the beamline. Multiple sets of grips were manufactured so that several specimens can be transported to the beamline in one shipment. Then, one specimen was mounted into the furnace chamber at a time for the *in situ* test.

Supplementary radiation shielding was used to minimize personnel exposure to radiation during the transport of the grip assembly and its installation inside the furnace, as shown in Fig. 28(b). The supplementary radiation shield is made of a tungsten tube with a wall thickness of 10 mm secured inside a stainless steel shell structure. The shell structure is designed for quick assembly and removal of the radiation shield. The supplementary radiation shield was removed after specimen installation prior to closing the chamber door, and was re-assembled inside the chamber before removing the specimen-grip assembly from the chamber.

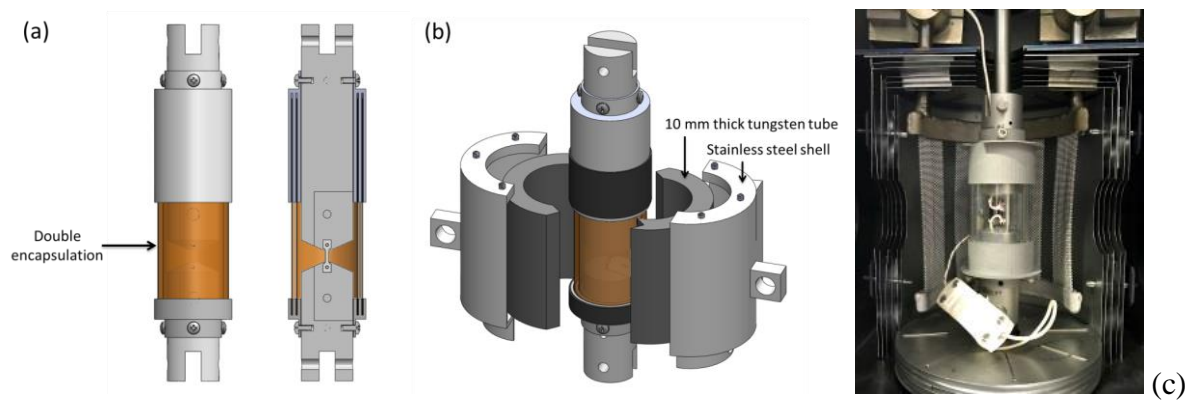


Figure 28. (a) The Krypton gripping assembly for a room temperature test of an activated specimen, (b) the double-encapsulated gripping assembly with the supplementary radiation shielding, and (c) the quartz double-encapsulated gripping assembly for an elevated temperature test of an activated specimen.

Four *in-situ* tensile tests were carried out: an irradiated specimen and an unirradiated control specimen were tested at room temperature in air, and an irradiated specimen and an unirradiated specimen were tested at 400°C in vacuum (10^{-5} Torr). All the tensile tests were conducted at a strain rate of $1-5 \times 10^{-5}$ /s. For elevated temperature tests, the specimens were heated under vacuum with the built-in tungsten heating elements. Two K-type thermocouples were embedded inside the top and bottom specimen grips, with their tips in close proximity to the specimen (Fig. 28(c)).

WAXS/SAXS measurements were conducted simultaneously with monochromatic X-rays in transmission while the specimen was under tensile deformation. The X-ray energy was 123 keV and the beam size was 0.2×0.2 mm². The specimen-to-detector distance was 3,135 mm, and the maximum 2θ was 9° , covering up to the 9th peak of the austenite phase ($\{224\}$). The WAXS signals were recorded with four GE amorphous Si area detectors (409.6 mm \times 409.6 mm active area with 2048×2048 pixels) arranged with a center hole for simultaneous SAXS. The number of grains in the illuminated volume was relatively small (< 50), due to the large grain size (about 150 μ m). To

increase the number of grains contributing to diffraction signals, a two-dimensional mapping scan over the specimen gauge was implemented. The specimens were translated along the gauge width direction while the diffraction data were continuously recorded using the so-called ‘fastsweep’ data collection mode. The specimen was also translated along the gauge length direction at multiple positions with a step size of 0.25 mm, and a “fastsweep” measurement was taken at each vertical position. During data analysis, diffraction patterns acquired at four steps in the vertical direction were summed and analyzed as one data point, which covers approximately 500 grains.

The data reduction and peak fittings were performed with a MATLAB[®] script provided by the Materials Physics and Engineering group of the APS. Instrument parameters (beam center, detector tilts, and specimen to detector distance) were calibrated using a CeO₂ standard specimen (NIST-SRM[®] 674b). Line profiles were generated by integrating the diffraction data for a specific range of azimuthal angle. The peaks were fit individually using the pseudo-Voigt function and a linear function as background. Transmission electron microscopy (TEM) was conducted to characterize the irradiation and deformation induced microstructural changes after *in situ* tensile tests.

Figure 29 shows the macroscopic true stress-strain curves (left), the (200) lattice strain parallel to the loading axis vs macroscopic true strain (middle), and the W-H slope values vs. macroscopic true strain (right) for the unirradiated and irradiated HT-UPS specimens tested at 20 and 400°C. The major findings were [8]:

- The macroscopic stress-strain curves show significant irradiation hardening and ductility loss. Irradiation hardening was mainly caused by irradiation induced Frank loops and their barrier strengths were estimated using the dispersed barrier hardening model at the two temperatures.
- The irradiated specimens exhibited a strong linear response of lattice strain evolution up to near the onset of the macroscopic yield, in contrast to the unirradiated specimens which showed an evident non-linear behavior well below the macroscopic yield. The room-temperature diffraction elastic moduli in the longitudinal direction were increased after irradiation, however, the 400°C diffraction elastic constants remained similar before and after irradiation.
- The lattice strain evolutions were anisotropic for all tested specimens. The evolution of the {200} lattice strain parallel to the loading axis ($\epsilon_{\{200\}}^L$) showed unique characteristics: $\epsilon_{\{200\}}^L$ at the micro-yield is an irradiation-sensitive, temperature-independent parameter; the evolution of $\epsilon_{\{200\}}^L$ in the plastic regime was temperature-dependent in the unirradiated HT-UPS specimens but temperature-independent in the irradiated specimens.
- The evolutions of the W-H slopes with strain in the irradiated specimens were nearly indistinguishable between tests at 20 and 400°C. In contrast, the W-H slopes were higher at 400°C than at 20°C in the unirradiated specimens.
- The evolution of $\epsilon_{\{200\}}^L$ matches well with the W-H slope (dislocation density) evolution with macroscopic strain in both unirradiated and irradiated specimens tested at 20 and 400°C. The evolution of $\epsilon_{\{200\}}^L$ and the W-H slope revealed the long-range internal stresses developed during tensile deformation
- The irradiated specimens followed similar work hardening paths as the unirradiated specimen macroscopically. After necking, the microstrain increased rapidly in the necking region in the irradiated HT-UPS.

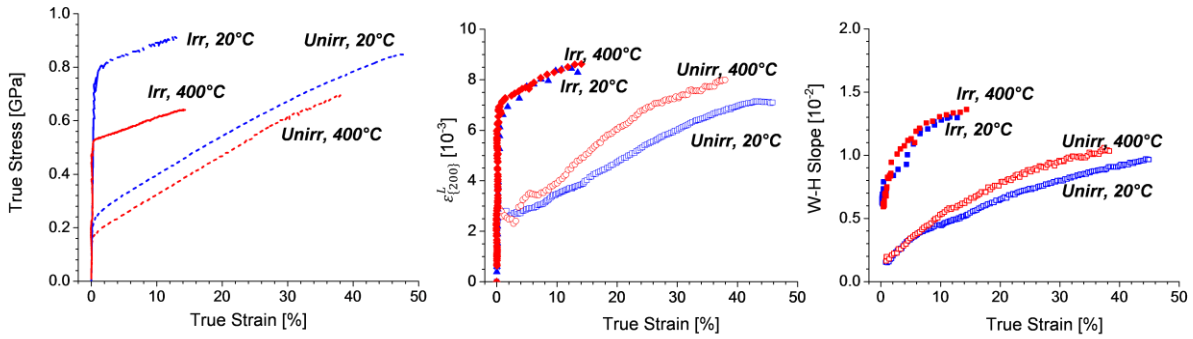


Figure 29. Macroscopic true stress-strain curves (left), the (200) lattice strain parallel to the loading axis vs macroscopic true strain (middle), and the W-H slope values vs. macroscopic true strain (right) for the unirradiated and irradiated HT-UPS specimens tested at 20 and 400°C.

4 Activated Specimens Handling and Proposed Activated Materials Laboratory (AML) at the APS

There has been growing interest in post-irradiation examination using advanced characterization tools at national user facilities such as the APS. Examining activated specimens at a public beamline at a national user facility is a challenging task due to radioactivity and contamination concerns. To mitigate exposure of personnel, equipment, and experimental station to radiation and contamination, radioactive specimens must be encapsulated at all times at the beamline facility. The specimen containment design can be expensive and time-consuming to develop, and the review process can be a lengthy process. In the past few years, we have developed a number of specimen holders and containments (some are shown in the previous sections), and related standard operating procedure for examining radioactive specimens at the APS. These specimen holder and containments have been approved by the APS Radioactive Specimen Safety Review Committee (RSSRC) and successfully demonstrated. This collection of radioactive specimen holder designs will be valuable to the nuclear community for conducting a range of synchrotron X-ray experiments safely on activated materials at the APS.

In this project, an effort was also made to implement automation of radioactive specimen handling. We acquired a Universal Robot UR5 AE3 and designed a specimen stage that can hold multiple individually-shielded and encapsulated radioactive specimens, as shown in Fig. 30. This specimen stage allows for handling multiple radioactive specimens by the Universal Robot for *ex situ* synchrotron X-ray measurements. The robot can be installed next to the specimen station inside a beamline hutch. It can be programmed with pre-defined motion steps such that it can lift one radiation shield at a time, pick up a radioactive specimen covered by the radiation shield from the specimen stage, and install the specimen on the X-ray specimen station. Once the measurement is completed, the robot can remove the specimen from the X-ray specimen station, return it to its original location on the specimen stage, and cover the specimen with its radiation shield. The robot can repeat the same loading/unloading scheme to handle the rest radioactive specimens. This automated specimen handling capability will significantly reduce radiation exposure of experimenters and increase efficiency and productivity.

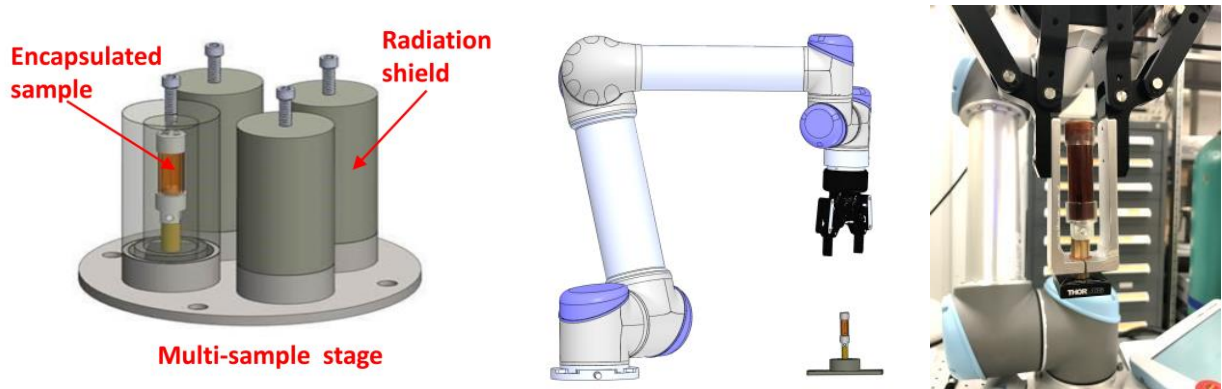
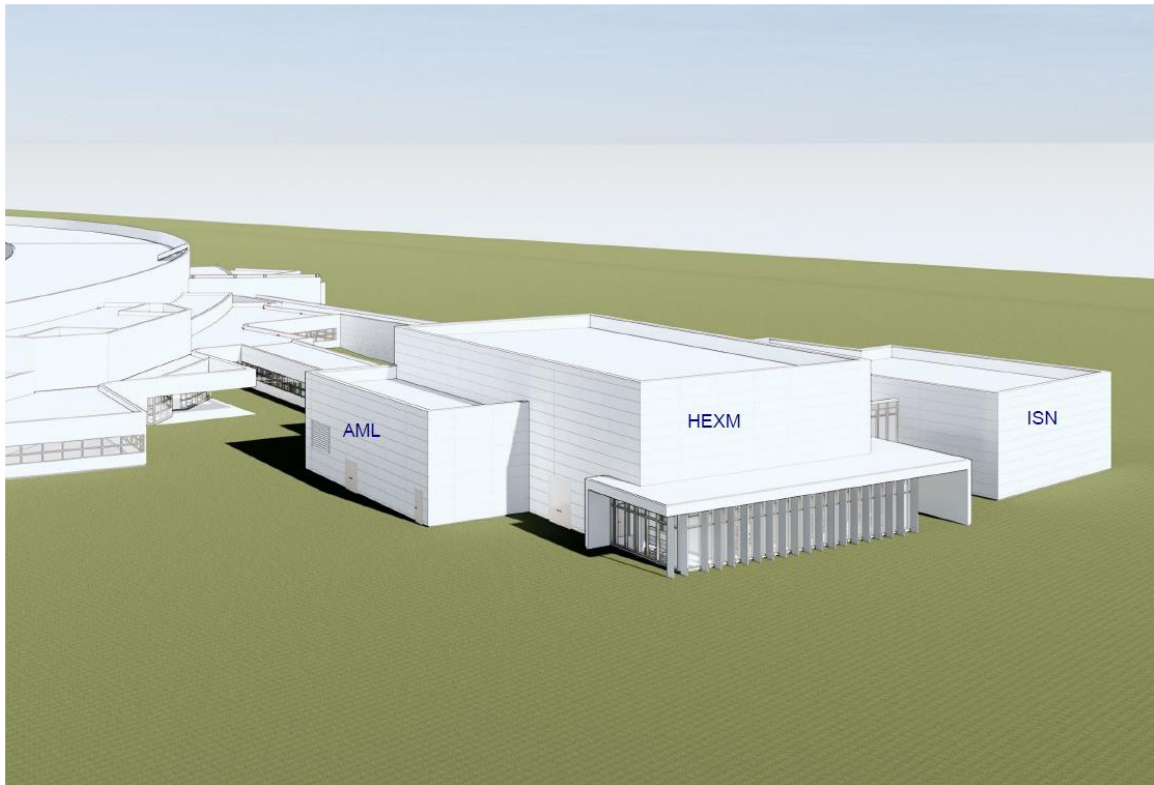


Figure 30. A 3D model of the radioactive specimen stage (left), a 3D model showing a robot handling a radioactive specimen (middle), and a photo taken during specimen loading showing the robot is gripping an encapsulated specimen holder (right).

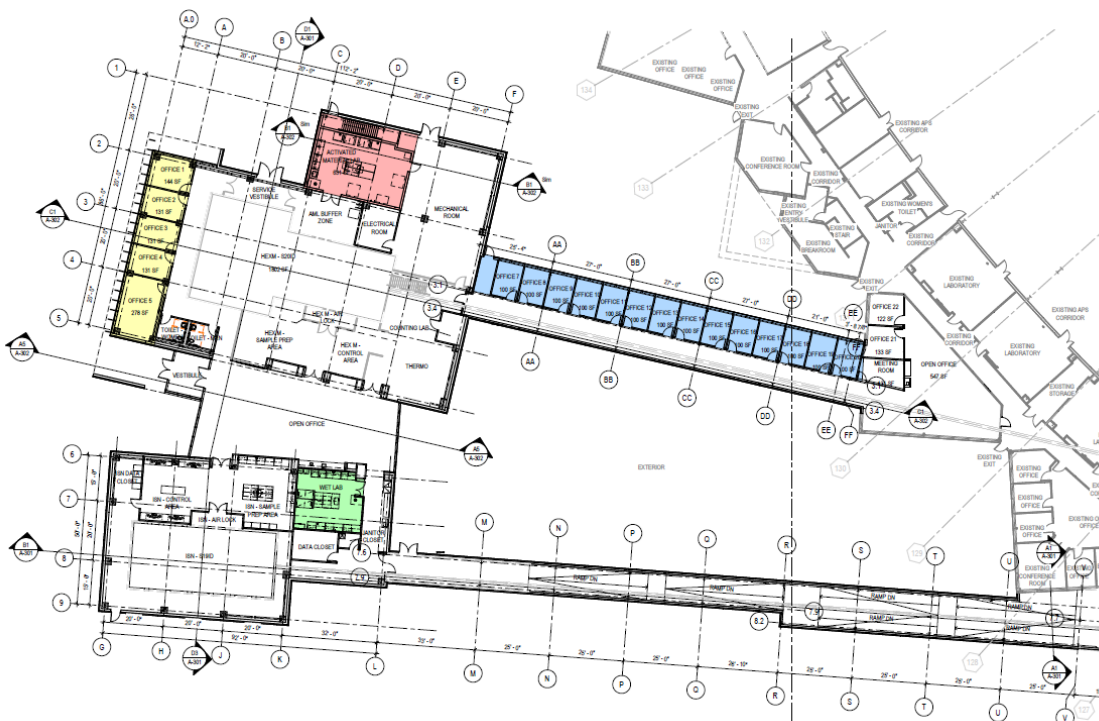
Our effort in developing capabilities for examinations of radioactive specimens at the APS in the past years has also led to a proposed Activated Materials Laboratory (AML). We proposed to build the AML, a radiological facility adjacent to the High-Energy X-ray Microscope (HEXM) beamline at the APS. The HEXM is a feature beamline to be built as part of the APS-Upgrade (APS-U) Project for investigations of structure and evolution within bulk materials in extreme environments. It will be equipped with both the enhanced high-energy X-ray scattering techniques used today (e.g., at APS 1-ID beamline) and with novel coherence-based techniques enabled by the low-emittance of APS-U multi-bend-achromatic (MBA) lattice. Part of the scientific scope of the HEXM beamline is to study nuclear reactor materials and fuels, some of which are radioactive and require appropriate handling as radioactive materials. The long beamline configuration of the HEXM and another new long beamline to be built, *in situ* nano-probe (ISN) requires a new building to house the experimental end stations for the ISN (at 19-ID) and the HEXM (at 20-ID) that will extend outside of the current APS Experiment Hall. The new building, known as the Long Beamline Building (LBB), is being designed and constructed by the APS-U. To facilitate handling of radioactive specimens at the HEXM, and to generally support work on radioactive specimens at the APS, the AML is proposed to be built within the LBB, as shown in Fig. 31.

The AML will be a Radiological Facility, per the DOE standards. It will allow for radioactive specimens to be safely prepared, handled, stored and transported while complying with all safety regulations. Materials to be handled in the AML are common nuclear structural and cladding materials and fuels in solid form, e.g. Fe-based alloys, Ni-based alloys, Zr alloys, refractory metals, ceramics, and uranium and uranium alloys. The main functions of the AML include (1) receiving and shipping activated specimens, (2) exposing and processing of open activated specimens such as assembling and disassembling specimen holder and containment in an enclosure, (3) characterizing, testing and maintaining experimental equipment for activated materials, e.g. microscopes, load frames, furnaces, chemical chambers, and other ancillary equipment used for *in situ* X-ray measurement, (4) short-term storage of activated specimens before and after the experiment. The AML will work in conjunction with Argonne's onsite radiological facilities for more involved specimen preparation work (e.g. sectioning, cutting, grinding, polishing, etc.). The AML will be accessible to qualified staff and users 24 hours a day, 7 days a week during run cycles. AML will provide improved specimen accessibility and flexible

operation, and minimize the rotation time between specimens, which will enhance scientific productivity, enable expansion of *in situ* testing capability, and maximize the use of HEXM and other beamlines at the APS.



(a)



(b)

Figure 31. AML within the Long Beamline Building (a) 3D model and (b) layout.

5 Summary

The project aims to develop a capability for conducting a multiscale experiment on an irradiated material enabled by high-energy X-rays by integrating *in situ* mechanical loading with a suite of high-energy X-ray techniques. The focus is on 3D microstructural characterization *in situ* to investigate grain dynamics in irradiated materials. A custom-made μ TS5 - 5 kN micro test system was developed for conducting *in situ* tensile tests of radioactive specimens with 3D high-resolution far-field High-energy X-ray Diffraction Microscopy (ff-HEDM) and tomography at the beamline 1-ID at the Advanced Photon Source (APS). A case study on neutron-irradiated Fe-9Cr specimens is presented, including *ex situ* near- and far- field HEDM and tomography before *in situ* tensile tests, *in situ* tensile tests with ff- HEDM and wide-angle X-ray scattering (WAXS), and *ex situ* near- and far-field HEDM and tomography after *in situ* tensile tests for neutron-irradiated Fe-9Cr specimens. Also discussed is *in situ* elevated-temperature tensile tests of a neutron-irradiated high-temperature, ultrafine-precipitate strengthened (HT-UPS) stainless steel using the *in situ* **Radioactive Materials** (iRadMat) characterization apparatus. These new capabilities open up new opportunities for the nuclear material community to study complex reactor materials at multiple length scales, allowing for bridging a wide range of length scales that are inherent in the deformation and failure processes in irradiated materials. We also proposed to build an Activated Materials Laboratory (AML) next to the new long beamline, High-Energy X-ray Microscope (HEXM) at the APS, as part of the APS-Upgrade Project. The AML will facilitate the access to these advanced characterization tools by the nuclear community.

Acknowledgement

This work was supported by the U.S. Department of Energy, Office of Nuclear Energy, for the Nuclear Energy Enabling Technology program under Contract DE-AC02-06CH11357. The neutron irradiated specimens were provided by the Nuclear Science User Facilities at the Idaho National Laboratory (INL). Use of the Advanced Photon Source (APS), Argonne National Laboratory (ANL) is supported by the U.S. Department of Energy (DOE), Office of Science under Contract DEAC02-06CH11357. Use of the Center for Nanoscale Materials, an Office of Science user facility, was supported by the U.S. Department of Energy, Office of Science, Office of Basic Energy Sciences, under Contract No. DE-AC02-06CH11357. The authors would like to express their appreciation to Ali Mashayekhi, Erika Benda, Roger Ranay at the APS for assistances with the experiments and engineering designs of specimen holders, Hemant Sharma at the APS for assistance in HEDM data analysis, Loren A. Knoblich and Yiren Chen at the Irradiated Materials Laboratory, ANL for handling and transferring irradiated specimens, Professor James Stubbins' group for sharing their Fe-9Cr neutron irradiated specimens, assistance with the APS experiments and analysis of HEDM data.

References

- [1] B.D. Wirth, G.R. Odette, J. Marian, L. Ventelon, J.A. Young-Vandersall, L.A. Zepeda-Ruiz, *J. Nucl. Mater.* 329-333 (2004) 103.
- [2] M.L. Young, J.D. Almer, M.R. Daymond, D.R. Haeffner, and D.C. Dunand, *Acta. Mater.* 55 (2007) 1999.
- [3] Leyun Wang, Meimei Li, Jonathan Almer, *Acta. Mater.* 62 (2014) 239.
- [4] M. Li, L. Wang, J. Almer, *Acta Mat.* 76 (2014) 381.
- [5] M. R. Daymond, M. L. Young, J. D. Almer, and D. C. Dunand, *Acta Mater.* 55 (2007) 3929.
- [6] U. Lienert, S.F. Li, C. M. Hefferan, et al, *JOM* 63 (2011) 70.
- [7] A. King, G. Johnson, D. Engelberg, W. Ludwig, and J. Marrow, *Science* 321 (2008) 382.
- [8] Chi Xu, Xuan Zhang, Yiren Chen, Meimei Li, Jun-Sang Park, Peter Kenesei, Jonathan Almer, Yong Yang, *Acta Mater.* 156 (2018) 330.
- [9] Xuan Zhang, Chi Xu, Leyun Wang, Yiren Chen, Meimei Li, Jonathan Almer, Erika Benda, Peter Kenesei, Ali Mashayekhi, Jun-Sang Park, and Frank Westferro, *Review of Scientific Instruments*, 88 (2017) 015111.



Nuclear Science and Engineering Division

Argonne National Laboratory

9700 South Case Avenue

Argonne, IL 60439

www.anl.gov